Supporting Information

1,5-Diiodocycloctane: a cyclane solvent additive can extend exciton diffusion length in thick film organic solar cells

Fengbo Sun, Xufan Zheng, Tianyu Hu, Jingnan Wu, Ming Wan, Yuanyuan Xiao, Tingting Cong, Yuda Li, Biao Xiao, Juan Shan, Ergang Wang, Xunchang Wang,* Renqiang Yang*

F. Sun, X. Zheng, T. Hu, Dr. M. Wan, Y. Xiao, T. Cong, Dr. B. Xiao, J. Shan, Dr. X. Wang, Prof. R. Yang
Key Laboratory of Optoelectronic Chemical Materials and Devices (Ministry of Education), School of Optoelectronic Materials & Technology, Jianghan University, Wuhan 430056, China
E-mail: wangxc@jhun.edu.cn, yangrq@jhun.edu.cn

J. Wu, Prof. E. Wang
Department of Chemistry and Chemical Engineering, Chalmers University of Technology, Göteborg 41296, Sweden

Dr. Y. Li
Key Laboratory of Novel Biomass-based Environmental and Energy Materials in Petroleum and Chemical Industry, Key Laboratory for Green Process of Ministry of Education, School of Chemical Engineering and Pharmacy, Wuhan Institute of Technology, Wuhan 430205, China

Materials and methods

Materials

Chloroform (Sigma-Aldrich, ≥ 99%), 1,8-diiodioctane (DIO, Sigma-Aldrich, 98%), and cyclooctane-1,5-diol (CAS:55343-44-7, Bidepharm, 98%) were purchased from commercial sources and used without further purification. PM6, PCE10, Y6, L8-BO, BTP-4F-P2EH, PYIT, PYF-T-o, IT-4F, and PDINN were obtained from Organtec Ltd., and D18 and PBQx-TF were purchased from Derthon Optoelectronic Materials Co., Ltd. DICO was synthesized as follows:

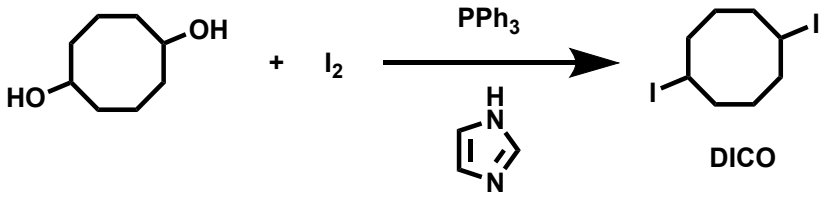

Scheme S1. The synthetic routes of DICO.

Synthesis of DICO

Triphenylphosphine (6 eq.) and imidazole (6 eq.) were dissolved in 30 mL of DCM and stirred until a homogeneous solution was obtained. Iodine (6 eq.) was then added slowly in portion and the resulting mixture was stirred until all iodine granules were dissolved. Cyclooctane-1,5-diol was then slowly added and the reaction mixture was stirred overnight at room temperature under a nitrogen atmosphere. The as-obtained brown solution was then diluted with hexane and filtered to remove the solid residues, and then the filtrate was concentrated under reduced pressure. The pale yellow solid was subsequently washed with hexane and filtered twice. The filtrate was then removed under reduced pressure and the crude product was purified by flash chromatography with silica gel using hexane as the eluent. DICO was obtained with a small amount of low boiling point impurities which were removed by vaccum heating. The resulting product was further purified by flash chromatography with silica gel using hexane as eluent to afford a pure DICO as a colorless liquid (yield 44%). ^{1}H NMR (400 MHz, $CDCl_3$) δ 4.59–4.53(m, 2H), 2.34–2.23 (m, 8H), 1.81–1.47 (m, 4H).

Methods

For nuclear magnetic resonance (NMR) spectroscopy, ^{1}H spectra were measured on a Bruker AV-500 MHz spectrometer in deuterated solvents at room temperature. Chemical shifts were recorded with tetramethylsilane (TMS) as the internal standard.

The UV–vis absorption spectra of the solutions and films were recorded using a Hitachi U-4100 spectrophotometer.

GIWAXS characterization was conducted by 2D-GIWAXS experiments using a GANESHA 300XL+ system from JJ X-ray. The instrument is equipped with a Pilatus 300K detector with a pixel size of 172 × 172 μm. The X-ray source is a Genix 3D M icrofocus sealed tube X-Ray Cu-source with an integrated monochromator (30 W). The wavelength used was λ = 1.5418 Å. The detector moved in a vacuum chamber with a sample-to-detector distance varied between 0.115 m and 1.47 m, depending on the configuration, as calibrated by silver behenate (d001 = 58.380 Å). The minimized background scattering plus high-performance detector allowed for a detectable q-range varying from 3×10^{-3} to 3 $Å^{-1}$ (0.2 to 210 nm). The sample was placed vertically on the goniometer and tilted to a glancing angle of 0.2° with respect to the incoming beam. A small beam was then used to obtain better resolution. The accumulation time was 30 min for each measurement. In-plane and out-of-plane line-cuts were obtained using the SAXSGUI program.

Atomic force microscopy (AFM) was performed through standard tapping-mode AFM measurements in ambient air on a scanned probe imaging and development (SPID) Park NX-10 imaging system. The AFM images were confirmed from different samples and scan areas. The root-mean-square roughness (RMS) values of the height images were obtained from the entire scan area (2 × 2 μm). All AFM images were flattened and exported from the software (XEI).

To obtain the surface electrostatic potential (ESP) and molecular polarity index**,** density functional theory (DFT) calculation were performed using the Gaussian 09 software package by selecting the 6-31G (d, p) basis set. The ground-state geometries were optimized using the popular B3LYP exchange-correlation functional, and ESP analysis was carried out using the wavefunction analysis tool Multiwfn. The surface electrostatic potential distribution diagrams of the non-fullerene acceptors were simulated with an electron density of 0.001 a.u. The molecular polarity index (MPI) of the acceptor molecules was calculated based on the distribution characteristics of the ESP on the molecular surface, with the value of MPI obtained as follows:

$$\mathrm{MPI} = (1/A)\iint |V(r)|dS \qquad (1)$$

where V is the electrostatic potential of the molecule, $\iint$ is the integration of the molecular surface S, and A is the molecular surface area, thus, the greater the MPI, the greater the overall polarity of the molecule. Since the non-uniformity of the charge distribution in the system reflects the polarity of the molecules, the more uneven the distribution, the more positive or negative regions of the electrostatic potential on the surface of

the molecule that would appear, making the MPI larger. The molecular polar surface area consisted of the area where the absolute value of the ESP was greater than 10 kcal/mol, and the molecular non-polar surface area was the area where the absolute value of the ESP was less than 10 kcal/mol.

Femtosecond transient absorption spectroscopy measurements were performed on an Ultrafast Helios pump-probe system in collaboration with a regenerative amplified laser system from coherent. An 800 nm pulse with a repetition rate of 1k Hz, a length of 100 fs, and energy of 7 μJ cm^{-2} $pulse^{-1}$ was generated by a Ti:sapphire amplifier (Astrella, Coherent). Subsequently, an 800 nm pulse was separated into two beams by a beam splitter, where one beam was coupled into an optical parametric amplifier (TOPAS, Coherent) to generate the pump pulses at various wavelength, while the other beam was focused onto a sapphire plate and a YAG plate to generate white light supercontinuum as the probe beams with the spectra covering 440–820 nm and 820–1200 nm, respectively. The time delay between the pump and probe was controlled by a motorized optical delay line with a maximum delay time of 8 ns. The pump pulse was sliced by a mechanical chopper with 500 Hz and then focused onto the mounted sample with probe beams. The probe beam was collimated and focused into a fiber-coupled multichannel spectrometer with CCD sensor, and the energy of the pump pulse was measured and calibrated by a power meter (PM400, Thorlabs). The samples used for TA measurements were obtained by spin-coating the neat and blended solutions on the quartz substrates.

The exciton annihilation method was used to estimate the diffusion length of each neat film. The series of fluence dependent decays were globally fit to rate equation accounting for the bimolecular (exciton annihilation) and monomolecular decay pathways, assuming that annihilation destroyed both excitons:

$$\frac{dn(t)}{dt} = -kn(t) - \frac{1}{2}\gamma n^2(t) \tag{2}$$

with the following solution:

$$n(t) = \frac{n(0)e^{-kt}}{1 + \frac{\gamma}{2k}n(0)(1 - e^{-kt})} \tag{3}$$

where $n(t)$ is the singlet exciton density as a function of time after the laser excitation, k is the monomolecular decay rate, and γ is the singlet-singlet bimolecular exciton annihilation rate. The intrinsic monomolecular decay constant, k, was extracted from the dilute neat film under weak laser irradiation (< 1 μJ/cm^{2}). The exciton decays could was well fitted by Eq. (3), where the only free parameter was the bimolecular rate constant. The bimolecular rate constant was then used

$$D = \frac{\gamma}{8\pi R} \tag{4}$$

to determine the 3D exciton diffusion coefficient, where D denotes the diffusion constant and R signifies the

effective interaction or annihilation radius of the singlet excitons, which consisted of the separation at which the annihilation occurred. A Förster radius for exciton-exciton annihilation of 4.8 nm was used following previous reports, which gave a 3D diffusion coefficient.

Time-of-flight secondary ion mass spectrometry (TOF-SIMS) was performed at PHI Nano TOF II TOF-SIMS (ULVAC-PHI, Japan) with Ar cluster as etching ion species. The films of ITO/PEDOT:PSS/PM6:L8-BO without and with the DIO and DICO additives was prepared following the procedure that used to fabricate real devices.

Contact angles were measured with a contact angle meter (GBX DIGIDROP). The solution of each organic material was spin-coated on cleaned ITO substrates. Droplets of H2O and CH_2I_2 were dripped onto the different films. According to Owens-Wendt method, surface tension could be divided into dispersive and polar components:

$$\gamma = \gamma^d + \gamma^p \tag{5}$$

Furthermore, the dispersive and polar surface tension can be calculated through the formula below based on the contact angles obtained by two solvents.

$$(1 + \cos\theta)\gamma_L = 2\sqrt{\gamma_S^d \gamma_L^d} + 2\sqrt{\gamma_S^p \gamma_L^p} \tag{6}$$

where θ is the contact angle of a specific solvent, γ_L is the surface tension of the solvent, γ_S^d and γ_L^d refer to the dispersive and polar surface tension of the solid, respectively, γ_S^p and γ_L^p refer to the dispersive and polar surface tension of the solvent, respectively. Thus, the unknown values γ_S^d and γ_L^p can be solved through combining two equations obtained by contact angle measurement of two different solvents.

Calculation of Flory-Huggins interaction parameter (χ) by contact angle Solubility parameter (δ) can be calculated from the surface tension:

$$\delta = K\sqrt{\gamma} \tag{7}$$

where γ is the surface tension, K is the proportionality constant (K =116×10^3 $m^{-1/2}$). Flory–Huggins interaction parameter (χ_{ij}) can be written as a function of two solubility parameter:

$$x_{ij} = \frac{V_0}{RT}(\delta_i - \delta_j)^2 \tag{8}$$

where χ_{ij} is the Flory–Huggins interaction parameter between the material i and j, V_0 is the geometric mean of the polymer segment molar volume, R is the gas constant, T is the absolute temperature, and δ_i and δ_j are the solubility parameter of material *i* and *j*, respectively. To simplify, we define the parameter

$$\kappa = K^2 V_0/RT \tag{9}$$

then the Flory–Huggins interaction parameter can be written as the formula below,

$$x_{ij} = k(\sqrt{\gamma i} - \sqrt{\gamma j})^2 \tag{10}$$

where γi and γj are the surface tension of material *i* and *j*, respectively.

Device characterization

The current-voltage (*J-V*) characteristics were measured by a Keithley 2450 source measurement system. The OSCs were measured under an irradiation intensity of 100 mW/cm^2 (AM 1.5 G) using a Newport solar simulator, where the effective area of the device was 0.042 cm^2. The EQE spectra were analyzed by an integrated system (LST-QE), while the high sensitive EQE was measured using an integrated system in which the photocurrent was amplified and modulated by a lock-in instrument.

Fabrication and characterization of single-carrier devices were conducted as follows. The hole and electron mobilities were calculated by the space charge limited current (SCLC) model with a device configuration of ITO/PEDOT:PSS/active layer/MoO_3/Ag and ITO/ZnO/active layer/PDINN/Ag, respectively, with the current density calculated as follows:

$$u = \frac{8}{9} \cdot \left(\frac{\sqrt{J}}{V}\right)^2 \cdot \frac{d^3}{\varepsilon_0 \varepsilon_r}, \tag{11}$$

where J is the current density, ε_o is the permittivity of free space, ε_r is the relative dielectric constant of the transport medium, μ is the hole mobility, and V is the voltage drop across the device:

$$V = V_{appl} - V_{bi} - V_{RS} \tag{12}$$

where V_{appl} is the applied voltage to the device, V_{bi} is the built-in voltage produced by the difference in the work function of the two electrodes, and V_{RS} denotes the voltage drop due to series resistance across the electrodes, and L is the thickness of the active layer.

Thermal admittance spectroscopy (TAS) measurements were conducted as follows. The test devices were fabricated using a conventional device structure of ITO/PEDOT:PSS/active layer/PDINN/Ag, which was consistent with the optimal solar cell device preparation conditions. Trap density of state (tDOS) was performed on a Keysight E4990A instrument and analyzed by the TAS method under angular frequency-dependent capacitance measurements (0.02 to 2000 kHz). The energetic profile of tDOS of the solar cells can be obtained from the following equation:

$$N_t(E_\omega) = -\frac{V_{bi}\, dC\ \ \omega}{qWd\omega k_B T}, \tag{13}$$

where k_B is the Boltzmann's constant, ω is the angular frequency, C is the capacitance, T is the absolute temperature, W denotes the depletion width, and V_{bi} is the built-in potential. The applied angular frequency ω

can be defined by the following formula:

$$E_{\omega} = k_B T \ln\left(\frac{\omega_0}{\omega}\right) \tag{14}$$

where ω_0 is the attempt-to-escape frequency. The trap states below the energy demarcation could capture or emit charges with the given ω and contribute to the capacitance.

Thin-film preparation and solar cell fabrication was carried out as follows. Indium tin oxide (ITO)-coated glass substrates were cleaned by sequential ultra-sonication in dilute Extran 300 detergent solution, deionized water, acetone, and isopropyl alcohol for 20 min each. These substrates were subsequently cleaned by UV-ozone treatment for 20 min, where copper (I) thiocyanate (CuSCN) (25 mg/mL) (Sigma-Aldrich) was dissolved in diethyl sulfide (DES) (Sigma-Aldrich) at 60°C for 1 h and then filtered. The CuSCN solution was spin-cast at 2500 rpm for 30 s, followed by annealing of the device at 105°C for 10 min. For the bilayer CuSCN/acceptor devices, the acceptors were dissolved in chlorobenzene (CB) at different concentrations (7–30 mg/mL) for ITIC and $PC_{71}BM$, or in chloroform (CF, 3–20 mg/mL) for Y6, L8-BO, A-C10ch, BTP-4F-P2EH, PY-IT, and PYF-T-o. The acceptor layers were then spun on the CuSCN layer at different speeds for 30 s to obtain the acceptor film with different thicknesses (5–150 nm), with the film thicknesses measured by a Tencor surface profiler. A 5 nm layer of Phen-NaDPO (DPO) as the electron-transport layer (ETL) and exciton blocking layer (EBL) was then spun from methanol solution (0.5 mg/mL) on top of the acceptor layer. Next, the samples were placed in a thermal evaporator for evaporation of a 100 nm-thick layer of Argentum evaporated at 5 Å/s, where the effective area of the tested solar cells was 0.042 cm^2.

Supplementary Figures

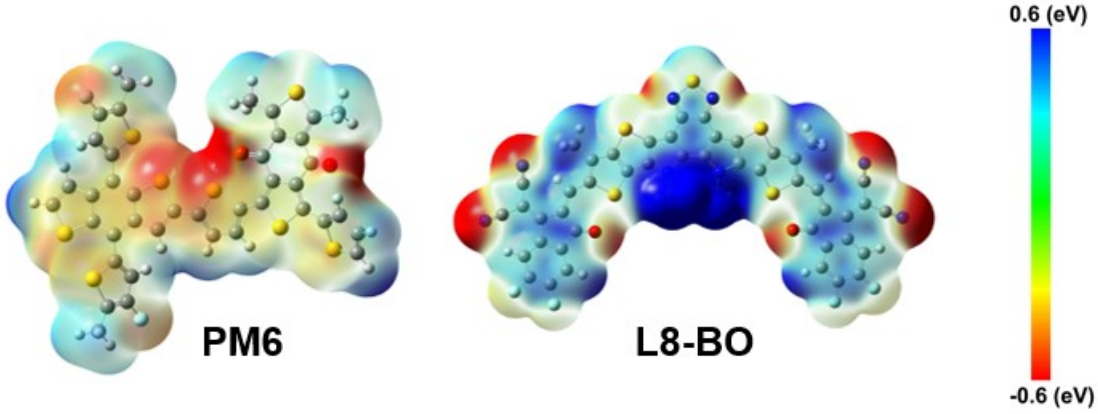

Fig. S1 Electrostatic potential (ESP) of the photovoltaic materials PM6 and L8-BO.

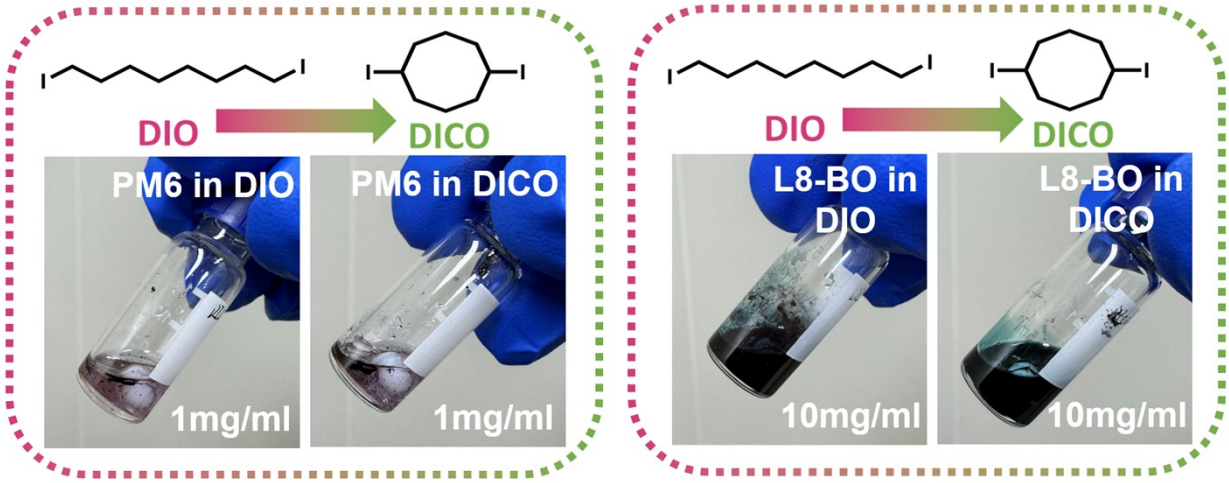

Fig. S2 The solubility test of the PM6 and L8-BO in DIO and DICO solvent additives.

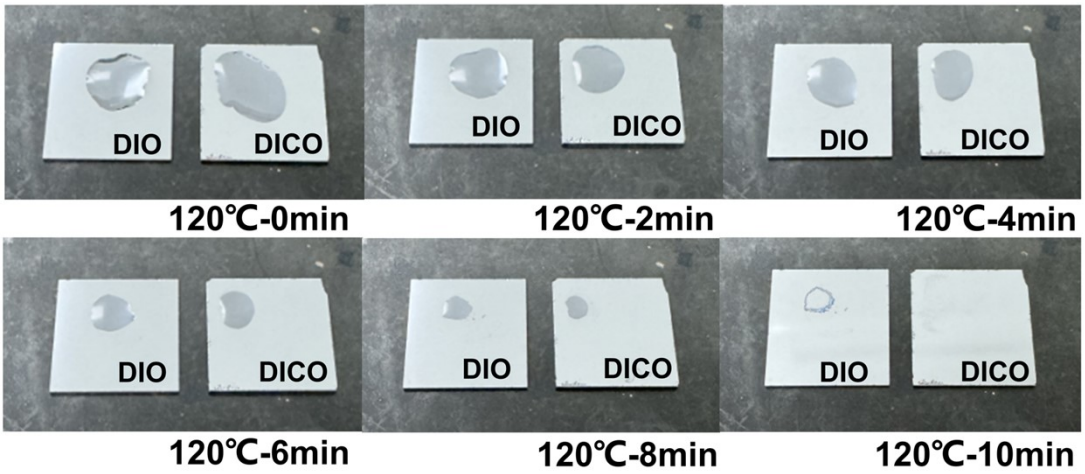

Fig. S3 The volatilization of DIO and DICO over time after dropping on a continuously heated silicon wafer.

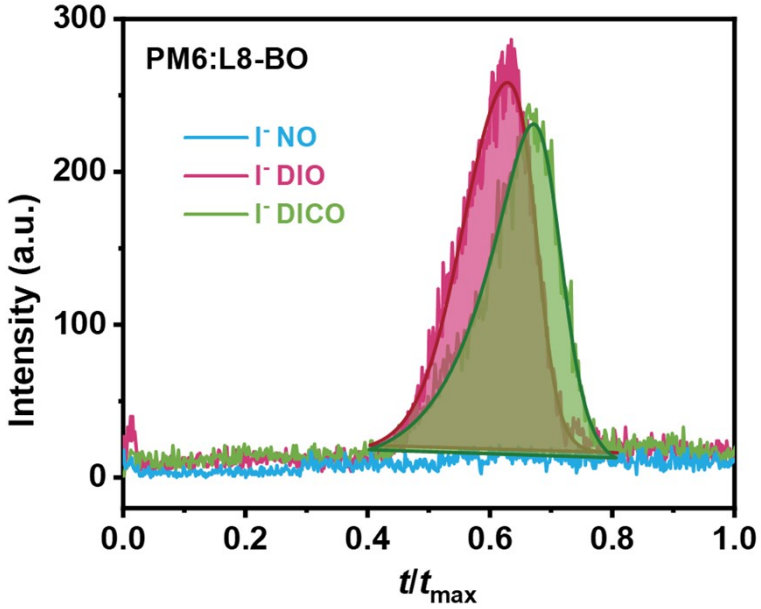

Fig. S4 Relative TOF-SIMS ion intensity of I^- based on the PM6:L8-BO blend films processed without and with the DIO and DICO additives.

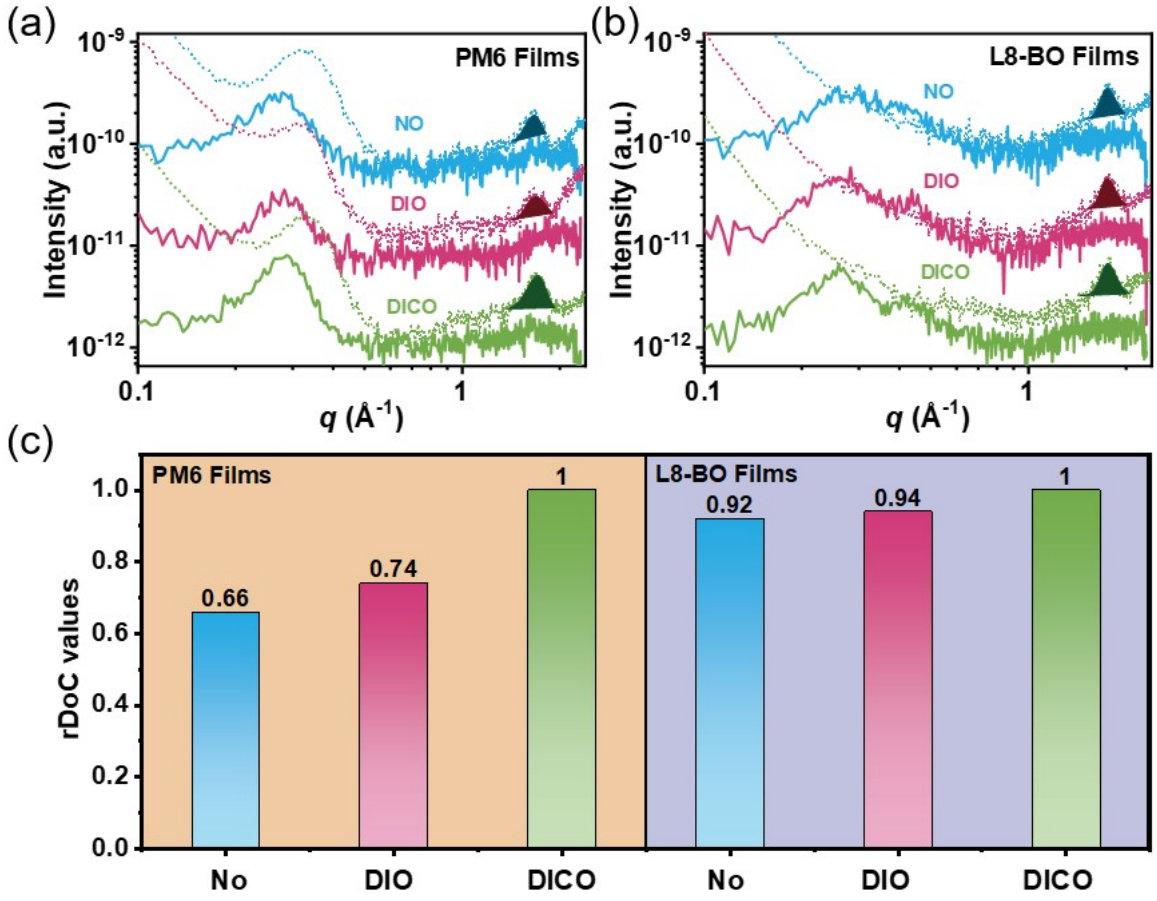

Fig. S5 Out-of-plane (dashed line) and in-plane (solid line) line-cut profiles of the GIWAXS patterns for the (a) PM6 and (b) L8-BO films processed without and with the DIO and DICO additives. (c) The rDoC values for the blend films processed without and with the DIO and DICO additives.

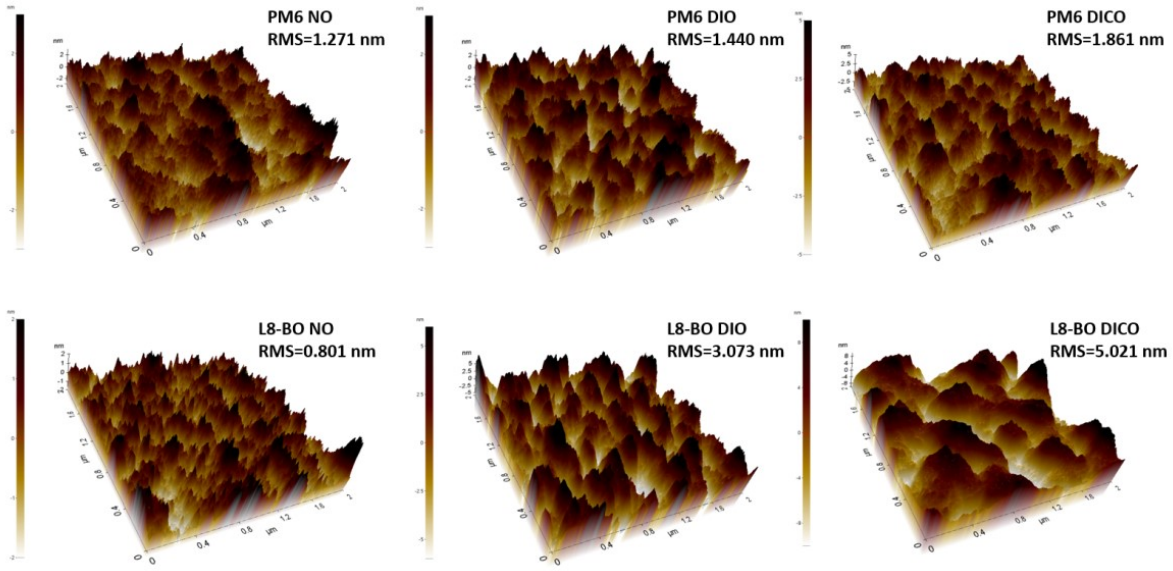

Fig. S6 AFM height images of the PM6 and L8-BO neat films processed without and with the DIO and DICO additives.

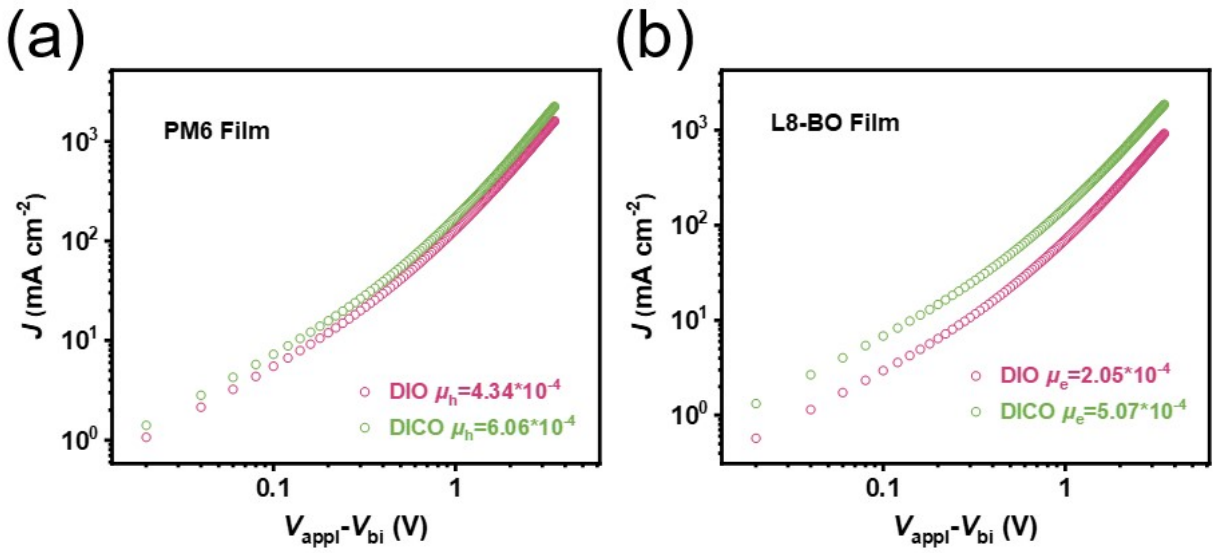

Fig. S7 SCLC curves of the (a) PM6- and (b) L8-BO-based devices processed with the DIO and DICO additives.

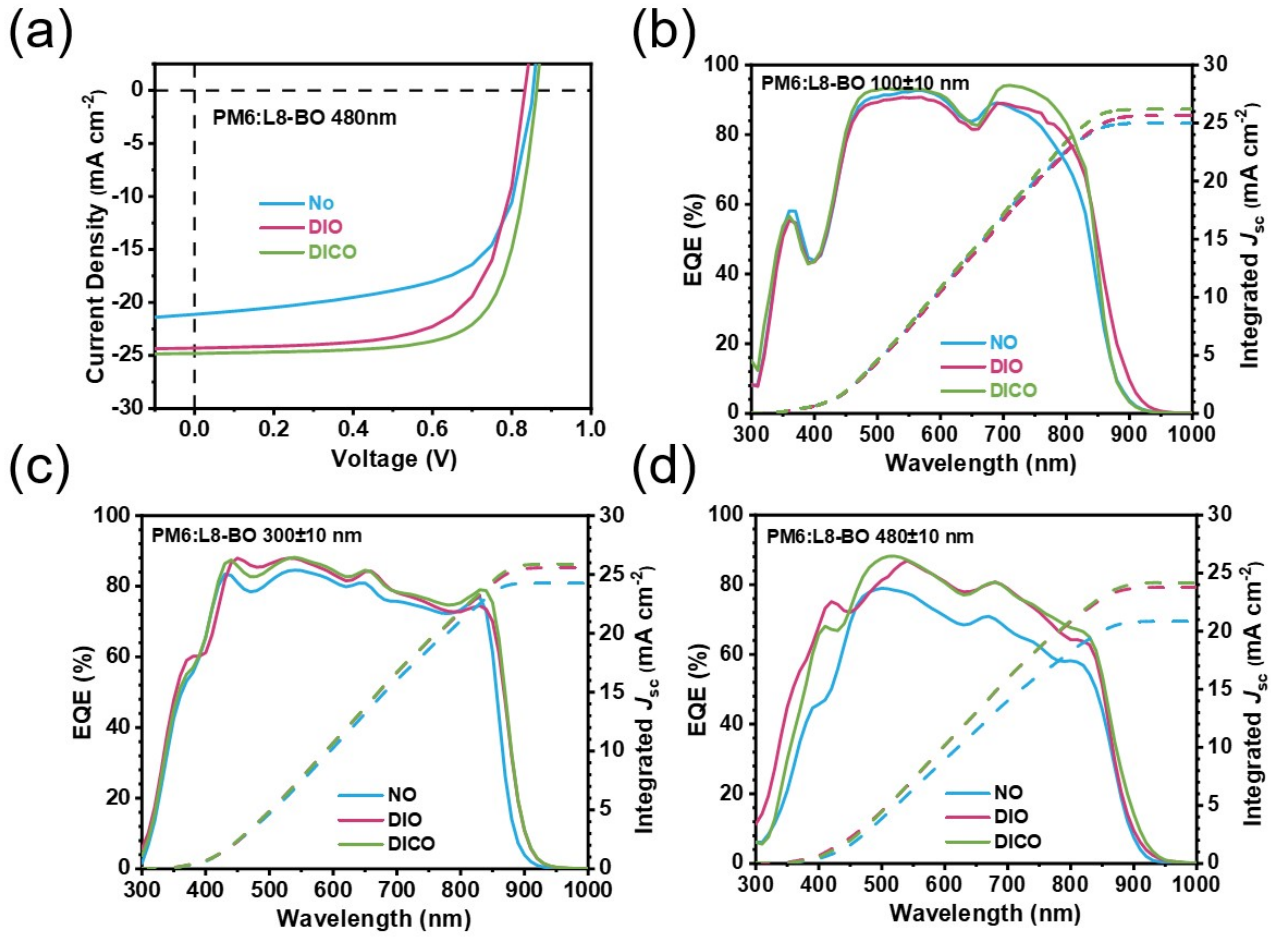

Fig. S8 *J-V* curves of the PM6:L8-BO-based devices processed with the DIO and DICO additives with (a) 480±10 nm active layers, where the EQE curves of the PM6:L8-BO-based devices processed without and with the DIO and DICO additives with (b) 100±10 nm, (c) 300±10 nm, and (d) 480±10 nm active layers.

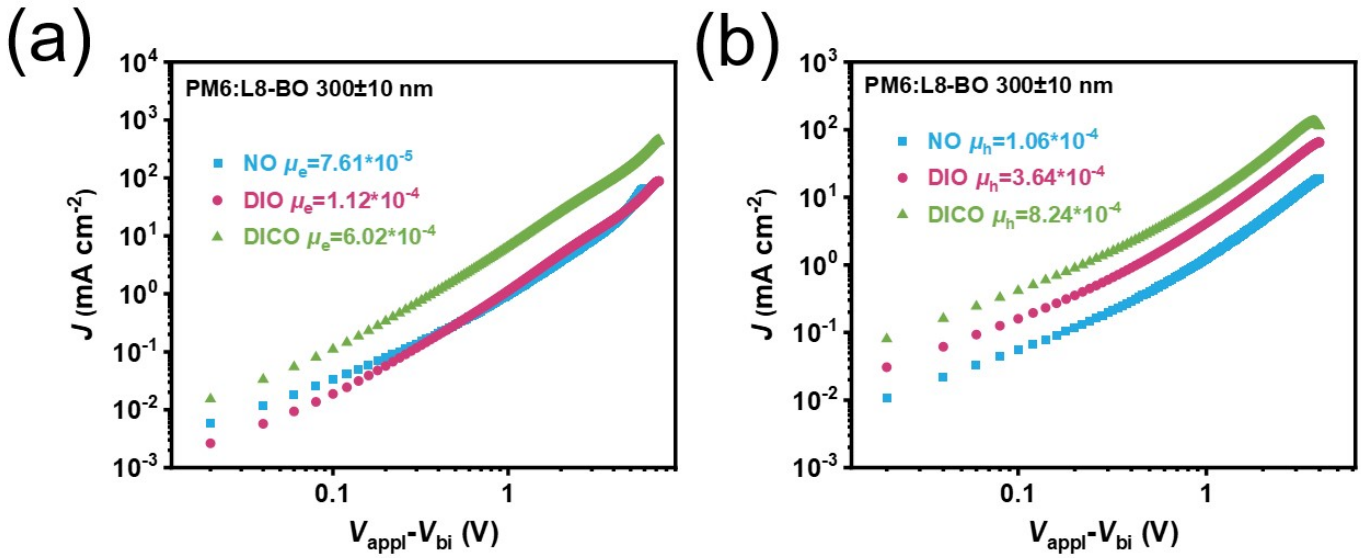

Fig. S9 (a) Current-voltage (*J-V*) characteristics of the optimized blend films in hole-only devices: ITO/PEDOT:PSS/blend film/MoO_3/Al; (b) Current-voltage (*J-V*) characteristics of the optimized blend films in electron-only devices: ITO/ZnO/blend film/Al.

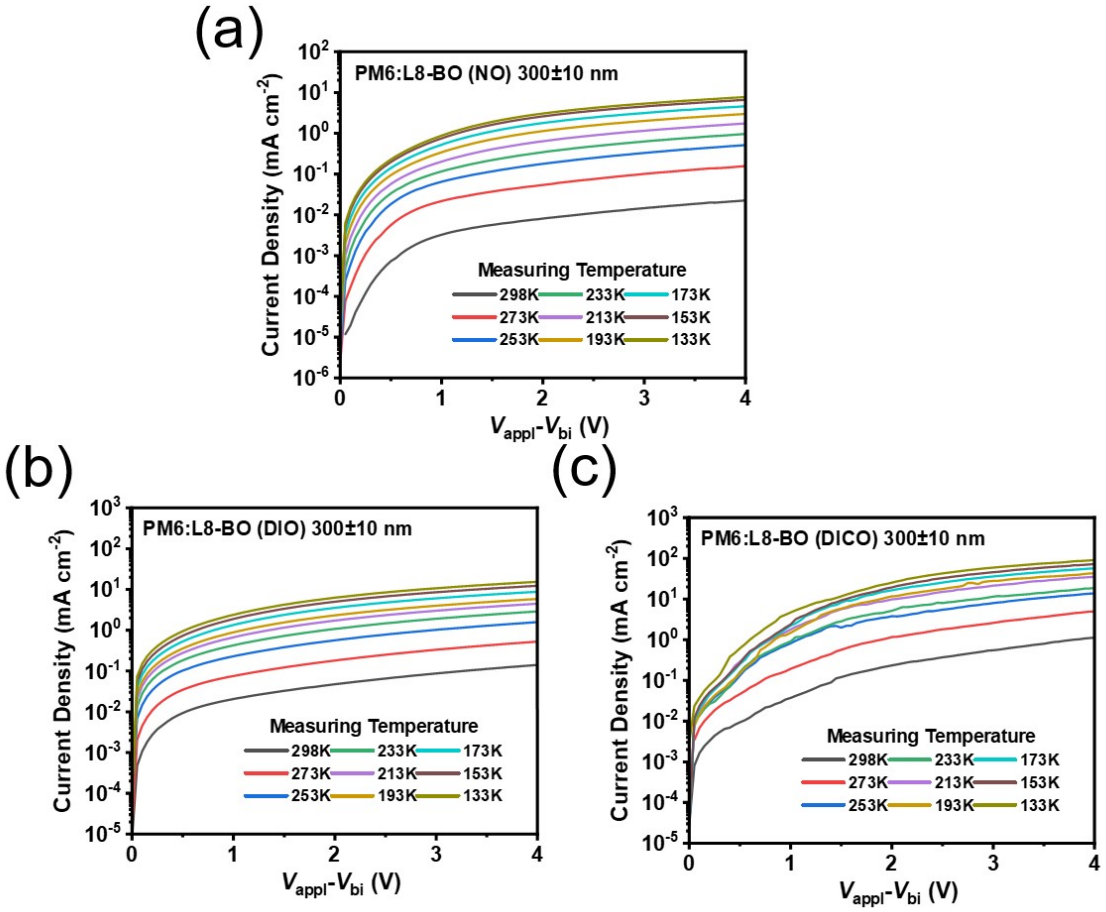

Fig. S10 Temperature dependent SCLC curves for PM6:L8-BO-based devices processed (a) without and with the (b) DIO and (c) DICO additives with 300±10 nm active layers.

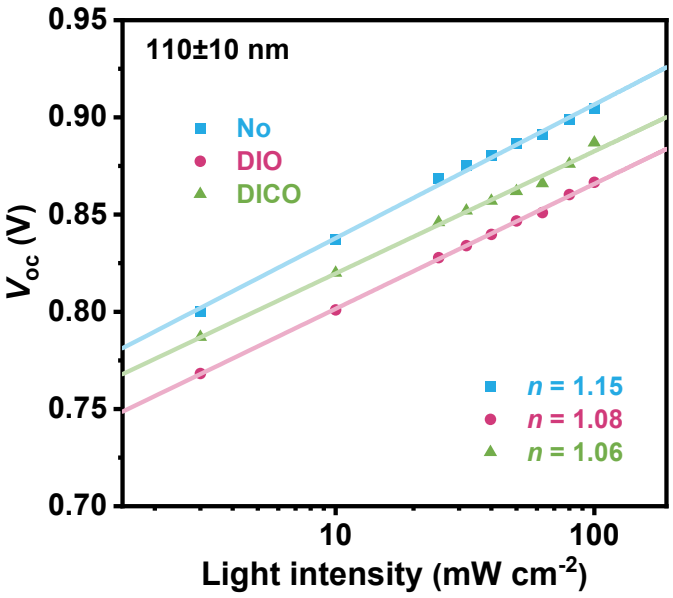

Fig. S11 V_{oc} versus light intensity plots of the thick film-based devices (110 nm) treated without additives and with DIO and DICO.

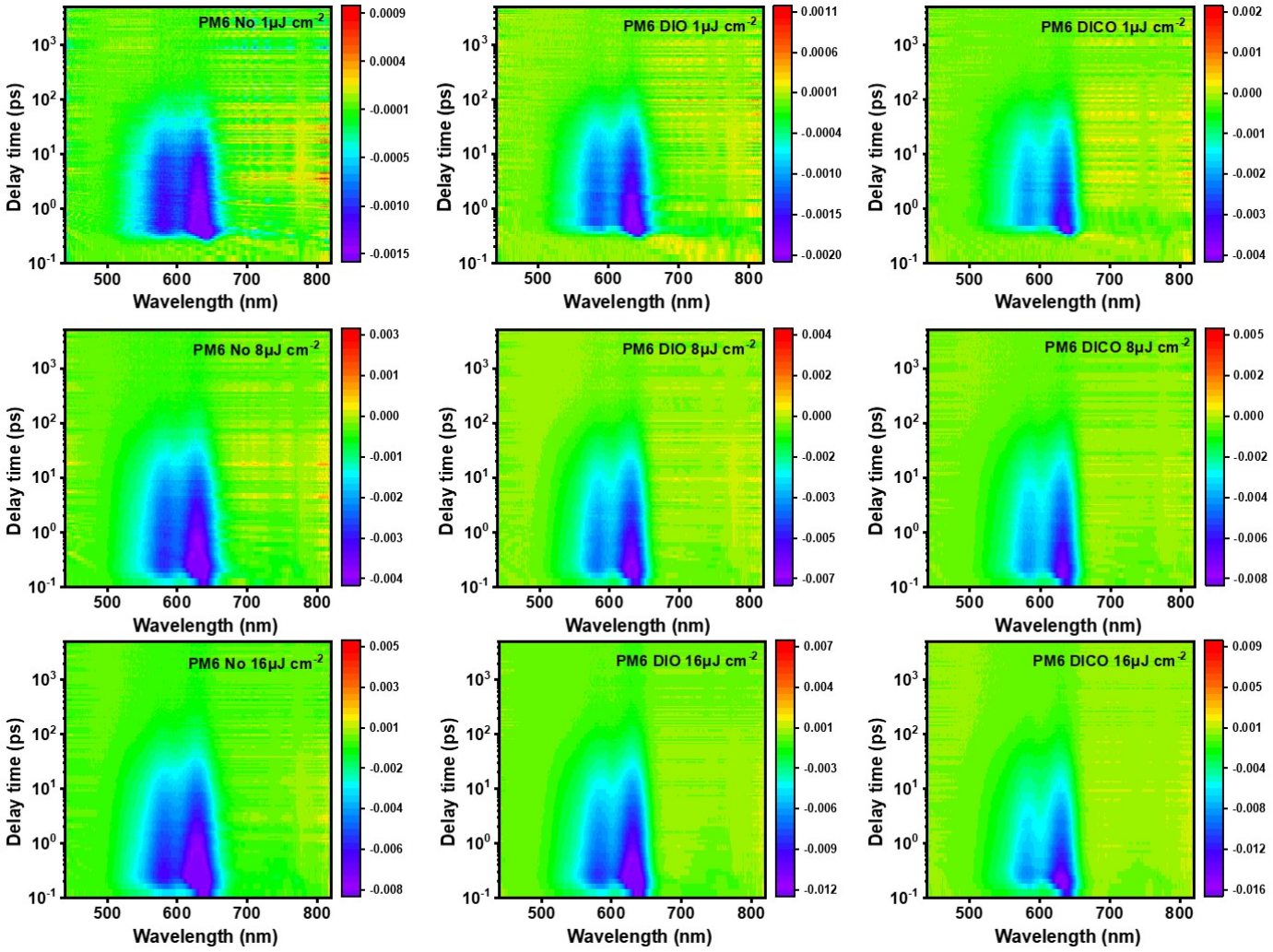

Fig. S12 The TA images of the PM6 neat film without additives and with DIO and DICO under 400 nm pump with power flux of 1, 8 and 16 μJ cm^{-2}.

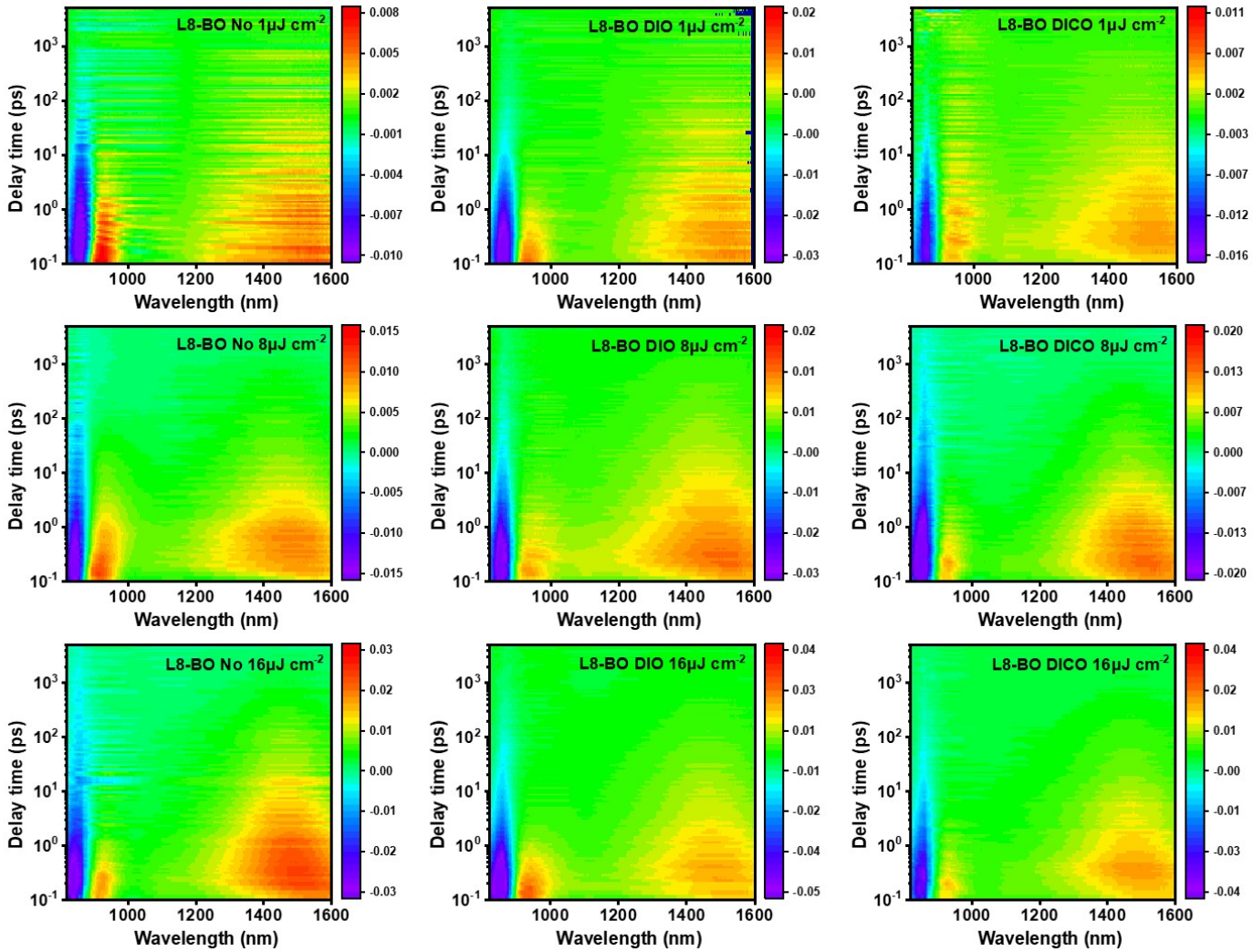

Fig. S13 The TA images of the L8-BO neat film without additives and with DIO and DICO under 800 nm pump with power flux of 1, 8 and 16 μJ cm^{-2}.

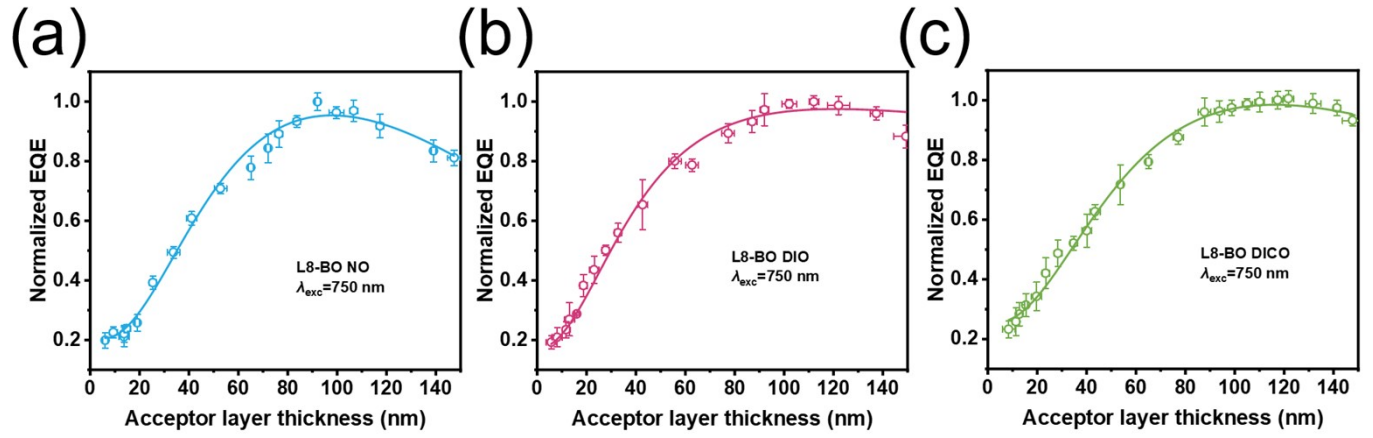

Fig. S14 EQE spectra of the CuSCN/NFA bilayer devices for the L8-BO layer thickness processed (a) without and with the (b) DIO and (c) DICO additives, measured using an excitation wavelength of λexc = 750 nm. The experimental data (circles) were fitted (solid lines) for all thicknesses.

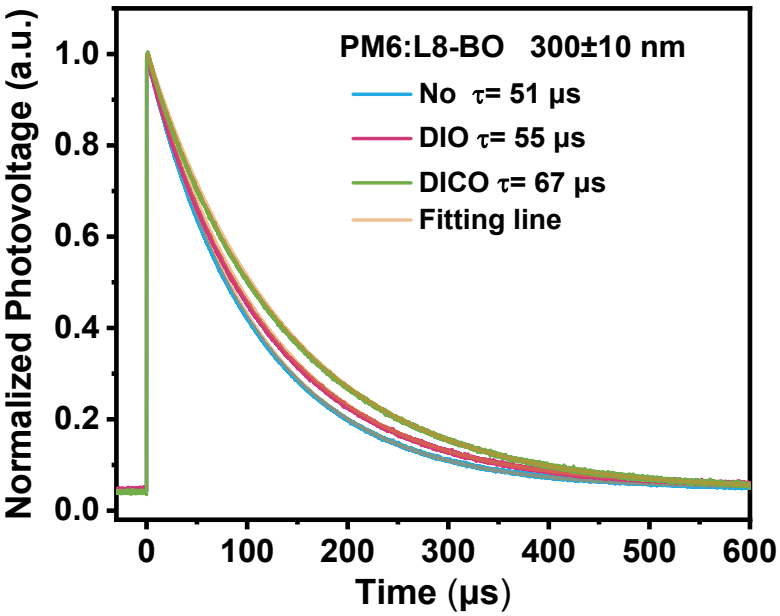

Fig. S15 Transient photovoltage measurements of the thick film-based devices (300 nm) treated without and with DIO and DICO additives.

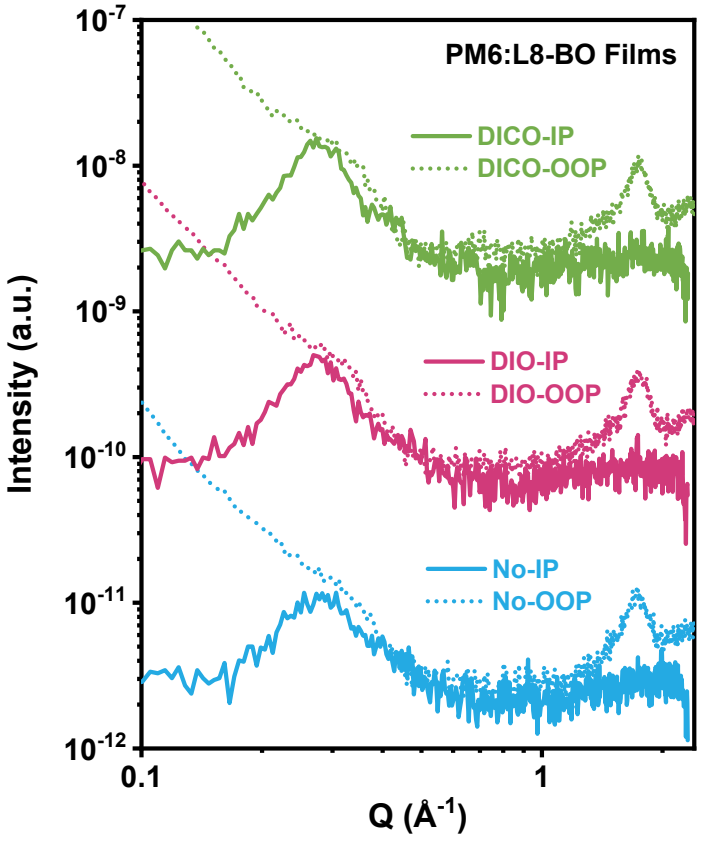

Fig. S16 Out-of-plane (dashed line) and in-plane (solid line) line-cut profiles of the GIWAXS patterns for the PM6:L8-BO blend films processed without and with the DIO and DICO additives.

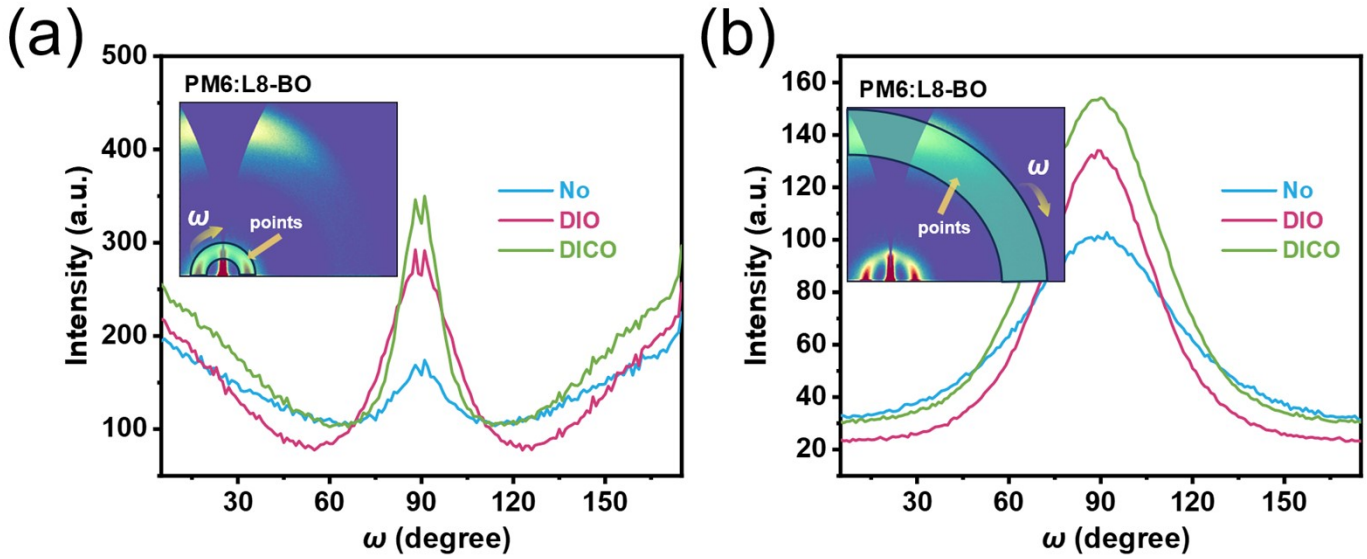

Fig. S17 Pole figure of the (100) peaks (a) and (010) peaks (b), where ω denotes the polar angle.

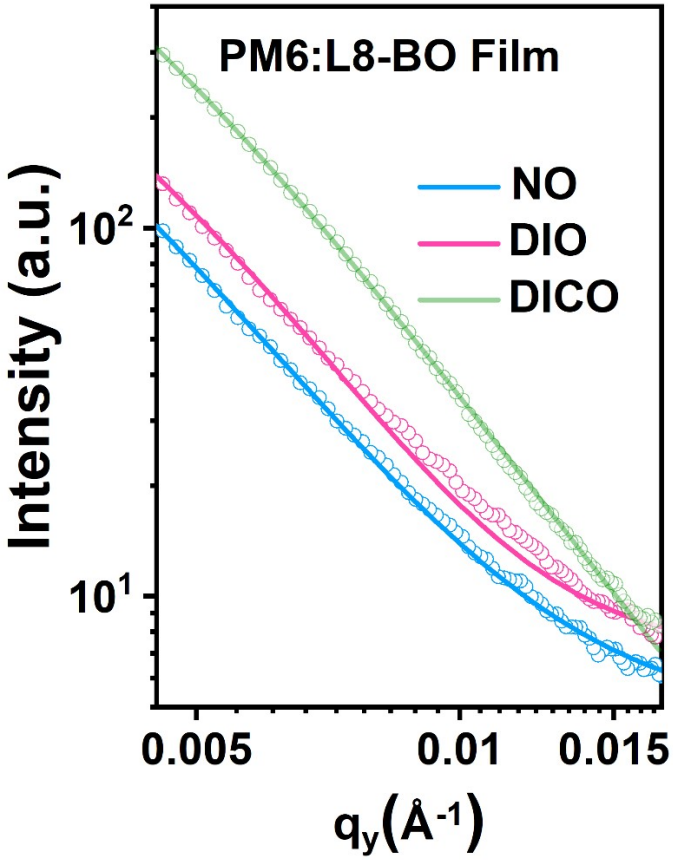

Fig. S18 GISAXS intensity profiles and best fittings along the in-plane direction of the PM6:L8-BO blended films without and with the DIO or DIMCH additives.

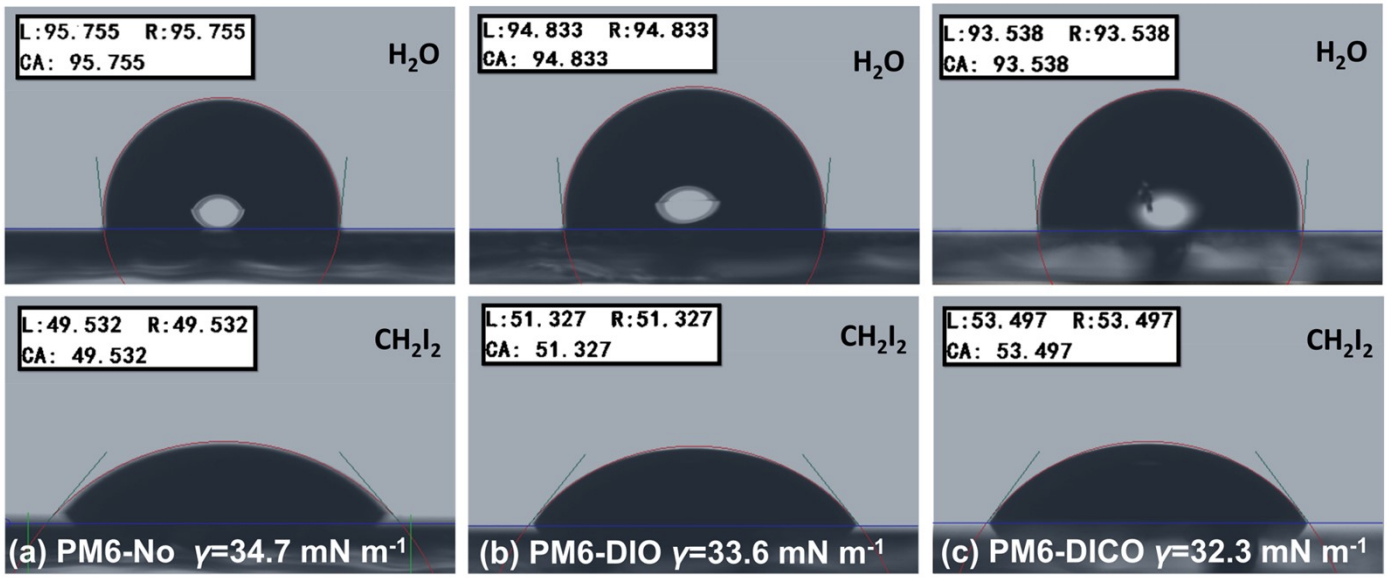

Fig. S19 Contact angle images of PM6 treated (a) without additive, (b) with DIO and (c) with DICO with H_2O and CH_2I_2 droplet on top of neat films.

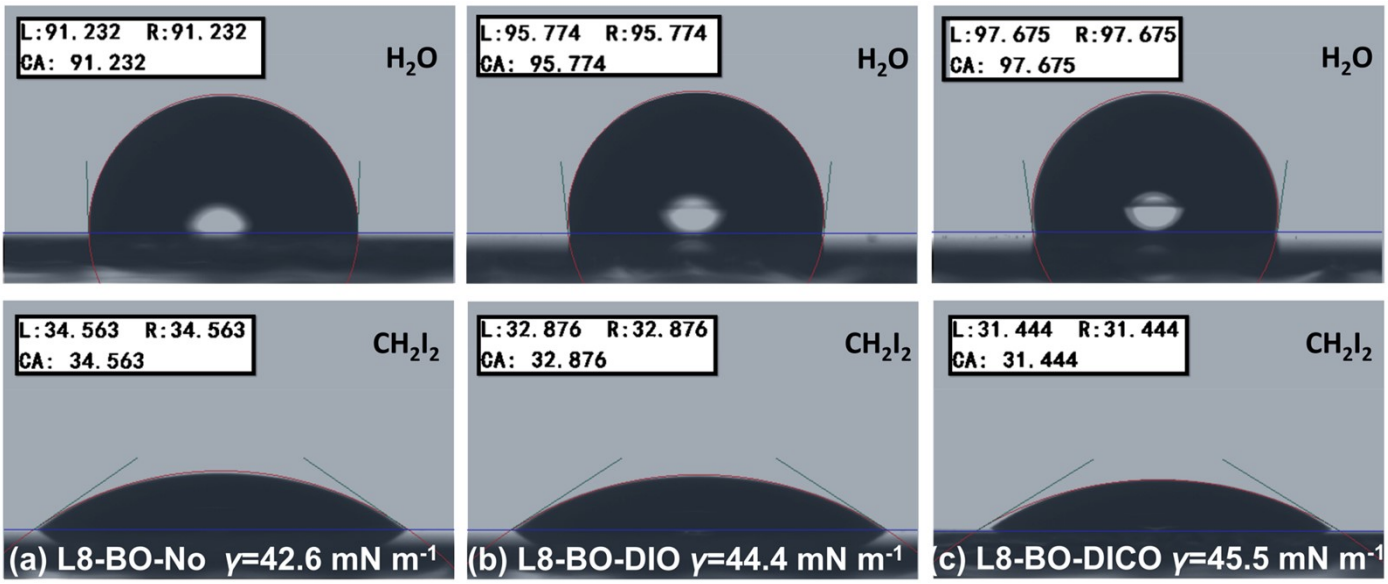

Fig. S20 Contact angle images of L8-BO treated (a) without additive, (b) with DIO and (c) with DICO with H_2O and CH_2I_2 droplet on top of neat films.

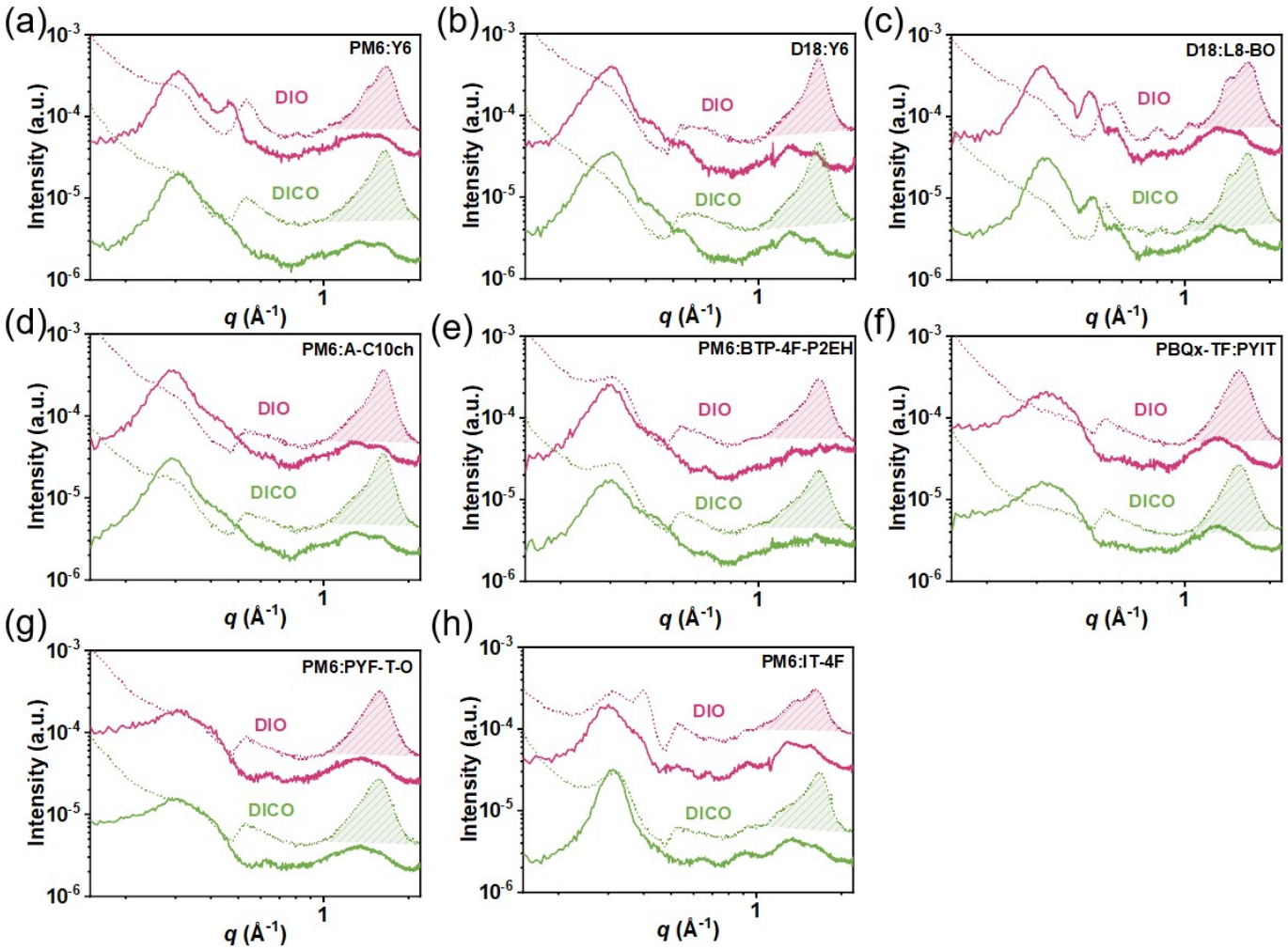

Fig. S21 Out-of-plane (dashed line) and in-plane (solid line) line-cut profiles of the GIWAXS patterns for the blend films processed with the DIO and DICO additives.

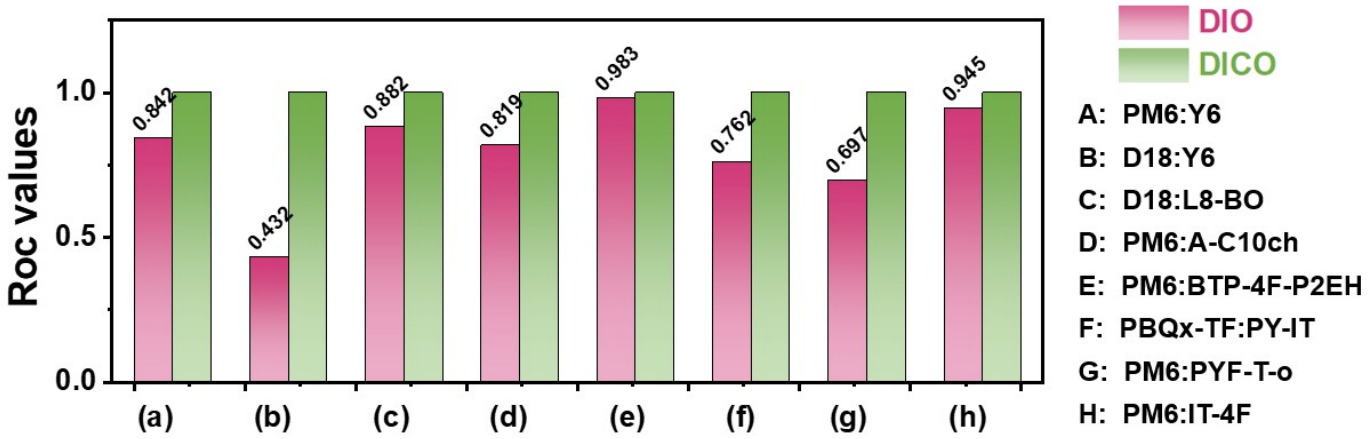

Fig. S22 The Roc values for the blend films processed with the DIO and DICO additives.

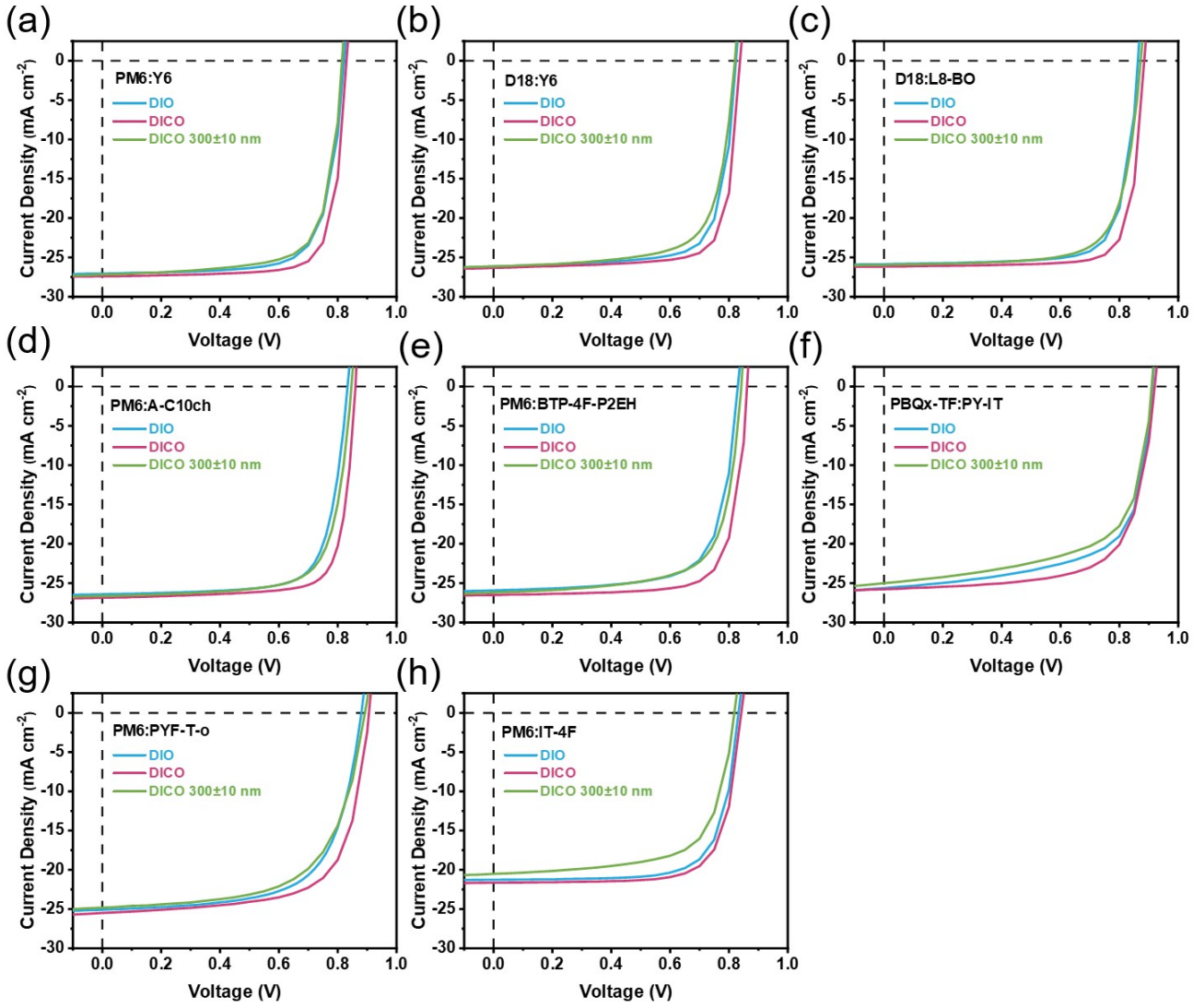

Fig. S23 a–i) *J–V* curves of optimized devices measured under AM 1.5G solar irradiation at 100 mW/cm^2.

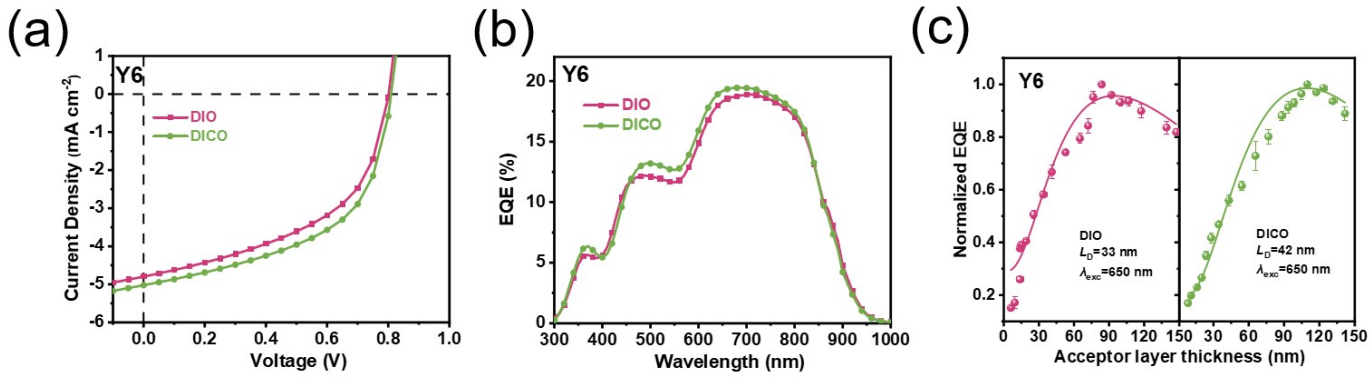

Fig. S24 (a) Current density–voltage (*J–V*) characteristics of OPV cells measured under simulated solar illumination; (b) corresponding EQE spectra of the bilayer OPVs; (c) EQE spectra of CuSCN/NFA bilayer devices for Y6 layer thickness processed with the DIO and DICO additives. The experimental data (circles) were fitted (solid lines) for all thicknesses.

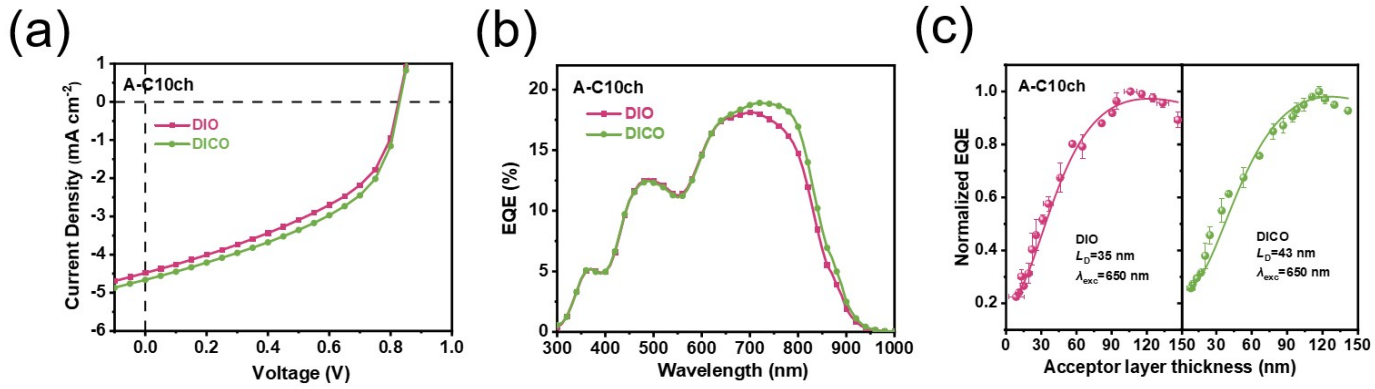

Fig. S25 (a) Current density–voltage (*J–V*) characteristics of OPV cells measured under simulated solar illumination; (b) corresponding EQE spectra of the bilayer OPVs; (c) EQE spectra of CuSCN/NFA bilayer devices for the A-C10ch layer thickness processed with the DIO and DICO additives. The experimental data (circles) were fitted (solid lines) for all thicknesses.

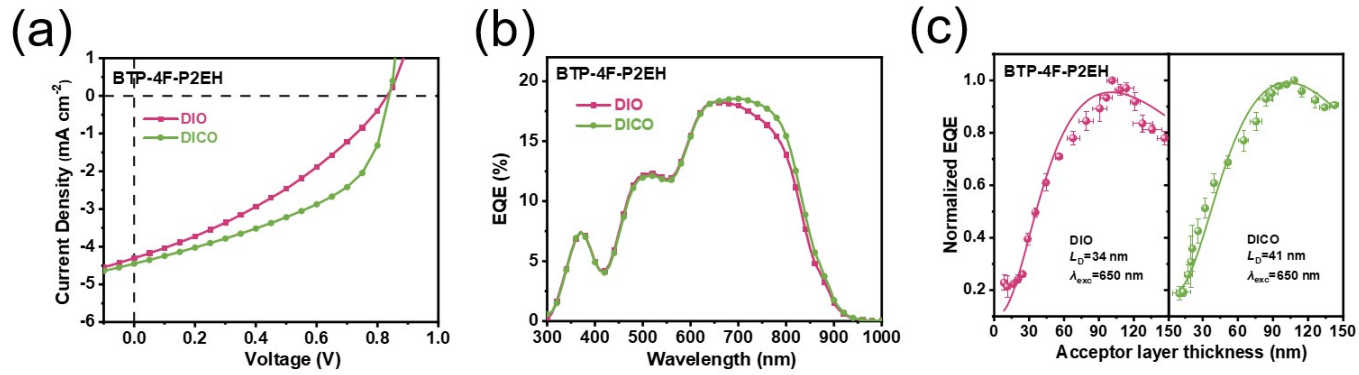

Fig. S26 (a) Current density-voltage (*J–V*) characteristics of OPV cells measured under simulated solar illumination; (b) corresponding EQE spectra of the bilayer OPVs; (c) EQE spectra of CuSCN/NFA bilayer devices for BTP-4F-P2EH layer thickness processed with the DIO and DICO additives. The experimental data (circles) were fitted (solid lines) for all thicknesses.

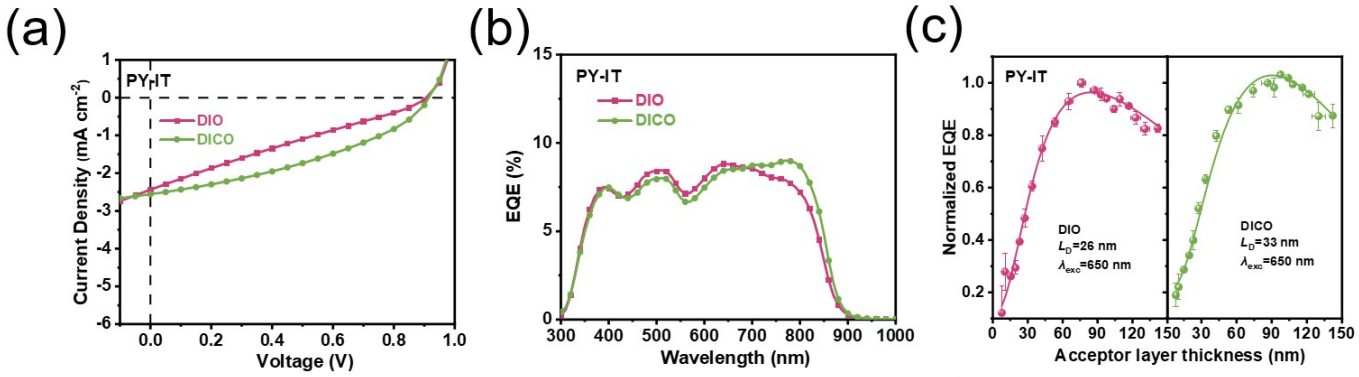

Fig. S27 (a) Current density-voltage (*J–V*) characteristics of the OPV cells measured under simulated solar illumination; (b) corresponding EQE spectra of the bilayer OPVs; (c) EQE spectra of CuSCN/NFA bilayer devices for the PY-IT layer thickness processed with the DIO and DICO additives. The experimental data (circles) were fitted (solid lines) for all thicknesses.

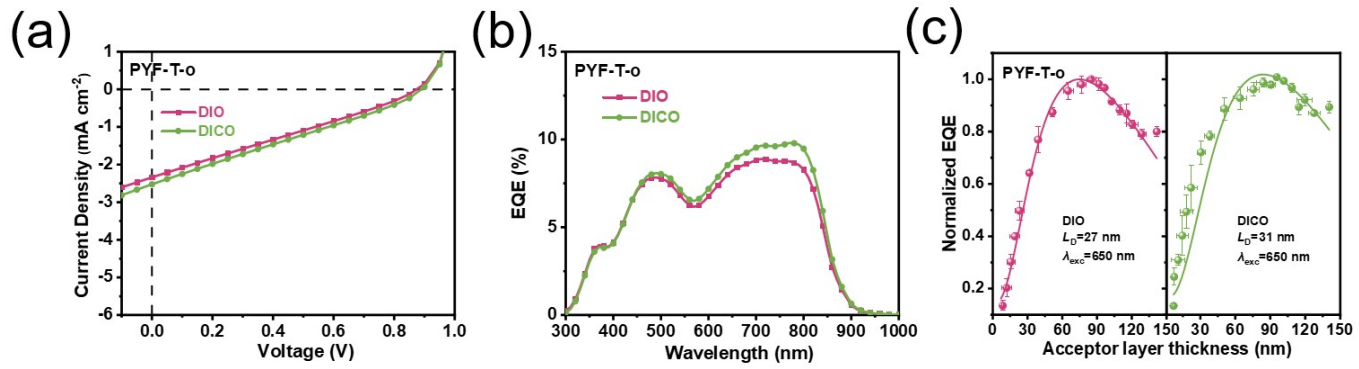

Fig. S28 (a) Current density-voltage (*J–V*) characteristics of the OPV cells measured under simulated solar illumination; (b) corresponding EQE spectra of the bilayer OPVs; (c) EQE spectra of CuSCN/NFA bilayer devices for PYF-T-o layer thickness processed with the DIO and DICO additives. The experimental data (circles) were fitted (solid lines) for all thicknesses.

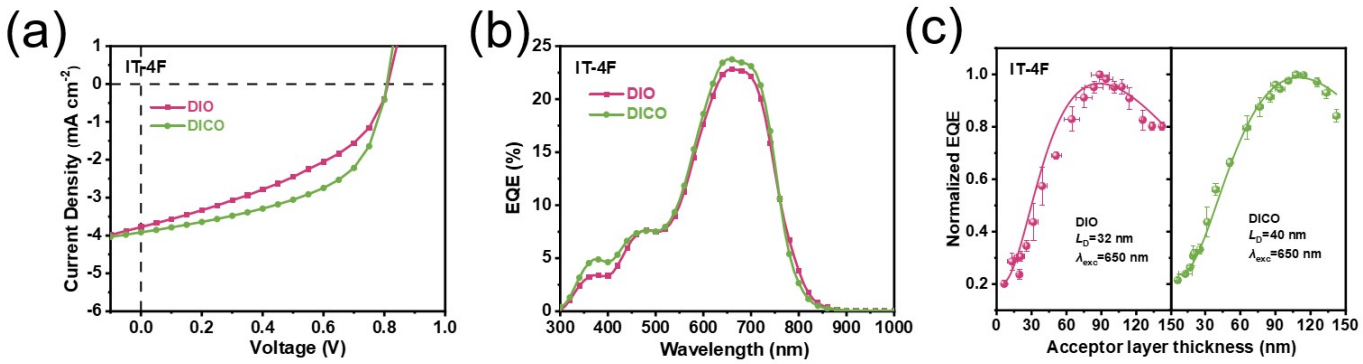

Fig. S29 (a) Current density-voltage (*J–V*) characteristics of OPV cells measured under simulated solar illumination; (b) corresponding EQE spectra of the bilayer OPVs; (c) EQE spectra of CuSCN/NFA bilayer devices for IT-4F layer thickness processed with the DIO and DICO additives. The experimental data (circles) were fitted (solid lines) for all thicknesses.

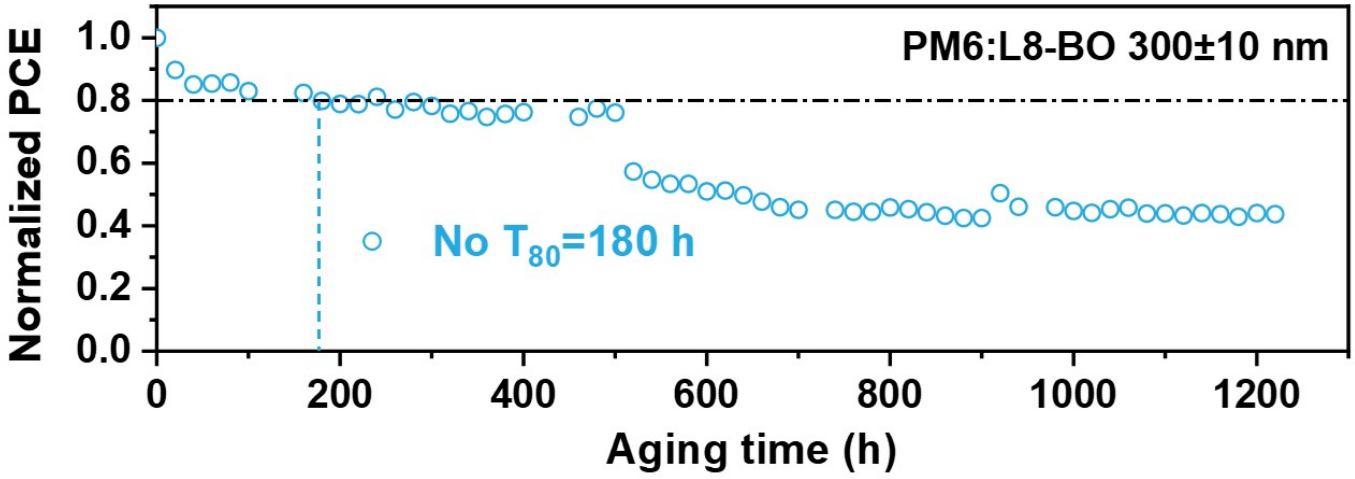

Fig. S30 Maximum power point (MPP) stability tests for the PM6:L8-BO-based devices without additive under 1-sun equivalent illumination from the white LEDs under MPP conditions in nitrogen atmosphere.

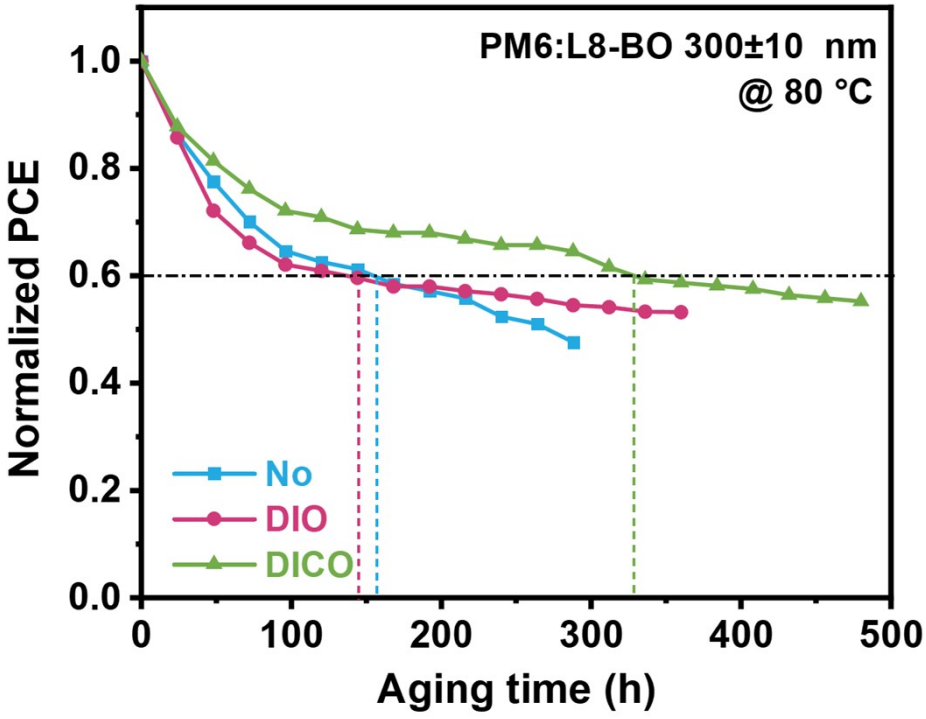

Fig. S31 Normalized PCEs of the PM6:L8-BO-based devices without additives and with DIO and DICO under long-term annealing at 80°C in a nitrogen-filled glovebox.

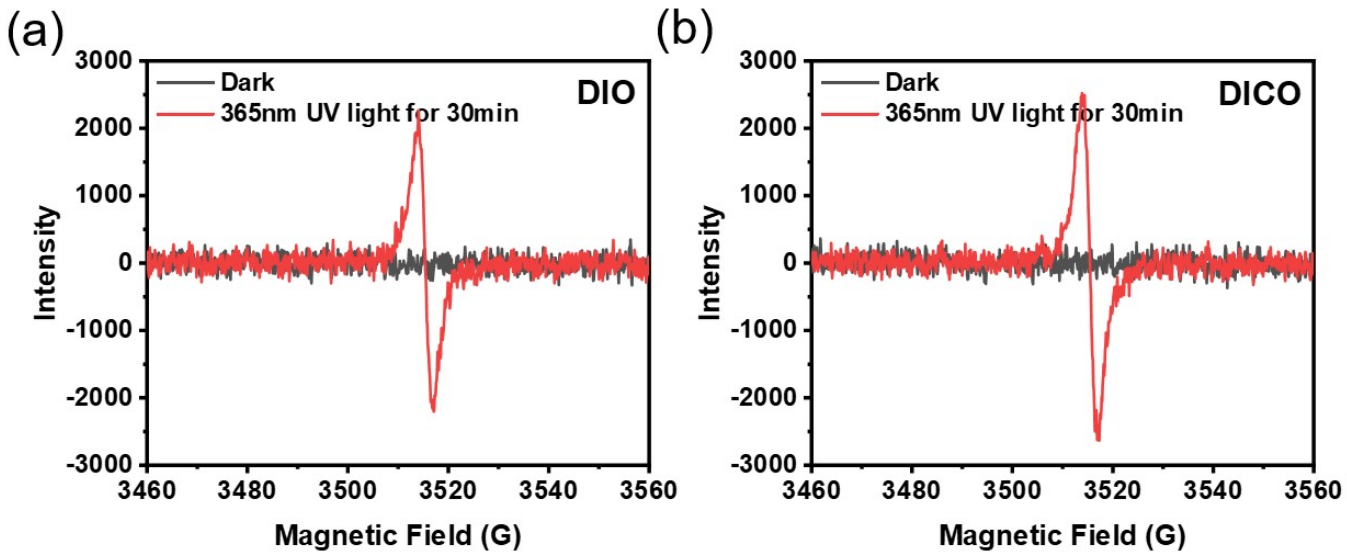

Fig. S32 Electron paramagnetic resonance spectra of solvent additives (a) DIO and (b) DICO.

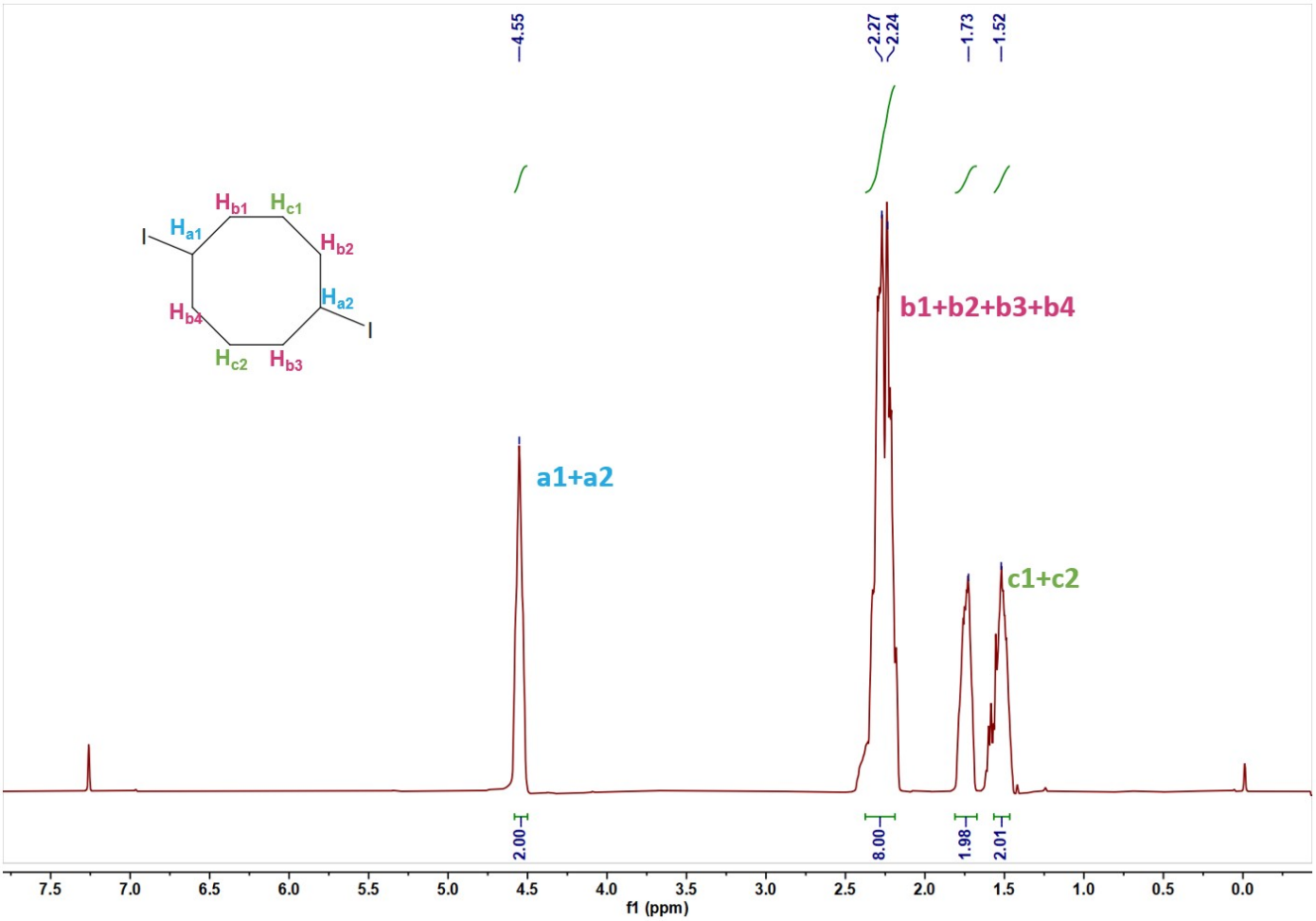

Fig. S33 [1]HNMR spectra of DICO.

Supplementary Tables

Table S1. Morphological information as revealed by GIWAXS investigations.

Additives	PM6				L8-BO			
	Q ($Å^{-1}$)	Distance (Å)	FWHM ($Å^{-1}$)	CCL (Å)	*Q* ($Å^{-1}$)	Distance (Å)	FWHM ($Å^{-1}$)	CCL (Å)
No	1.66	3.79	0.25	22.80	1.76	3.57	0.21	27.06
DIO	1.69	3.72	0.23	24.37	1.76	3.57	0.18	31.07
DICO	1.70	3.69	0.22	25.82	1.77	3.56	0.17	31.94

Table S2. Detailed device parameters of the reported representative thick-film OSCs.

Active layer	Thickness (nm)	J_{sc} [mA/cm^2]	V_{oc} [V]	FF [%]	PCE [%]	Ref.
P4TNT$_z$-2F:$PC_{71}BM$	350	19.45	0.82	66.5	10.62	1
PFBT4T-C5Si-25%:$PC_{71}BM$	420	19.08	0.76	74.12	11.09	2
PM6:IT-4F	285	22.6	0.83	64.8	12.2	3
PM7:MF2	500	19.20	0.953	54.9	10.04	4
PTQ10:IDTPC	400	17.90	0.913	61.3	10.0	5
Si25:IEICO-4F	320	26.87	0.70	70.15	13.2	6
PT2:TTPTTT-4F	400	20.5	0.87	56.5	10.1	7
	500	20.8	0.87	53.5	9.7	7
PBDB-T-2Cl:BTP-4F	300	27.6	0.821	54.1	12.2	8
PBDB-T:PJ1	305	21.1	0.87	65	12.1	9
PNTT:BTR:$PC_{71}BM$	280	20.88	0.75	70.67	11.44	10
PT2:TTPTTT-4F:IDIC	300	20.6	0.87	66.7	12.2	7
	400	21.5	0.86	65.3	12.4	7
	500	22.0	0.86	61.4	11.6	7
PBDB-T-2Cl:BTP-4F:$PC_{61}BM$	300	26.8	0.802	66.7	14.3	8
PBDB-T-2Cl:BTP-4F:MF1	300	23.06	0.882	71.62	14.57	11
PM6:Y6:BTP-M	300	26.87	0.855	62.06	14.23	12
BTR:NITI:$PC_{71}BM$	300	19.50	0.94	73.83	13.63	13
PM6:F-2Cl	350	19.73	0.866	58	10.00	14
	500	19.78	0.852	53	9.13	14

PffBT4T-2OD:$PC_{71}BM$	300	18.8	0.77	75	10.80	15
	320	24.92	0.782	74.69	14.55	16
Si25:Y14	390	24.53	0.782	73.68	14.79	16
	430	25.57	0.782	73.38	15.39	16
PNTT:$PC_{71}BM$	280	20.20	0.77	71.8	11.3	17
PBDB-T-2Cl:Y6:$PC_{61}BM$	300	26.8	0.802	66.7	14.3	8
PFBT4T-C5Si-25%:O-IDTBR	400	21.1	1.03	53.07	11.54	18
P2:IT-4F:BTP-4Cl	300	21.98	0.87	70	12.98	19
PBDB-TF:IDIC-C5Ph	470	20.15	0.921	70.12	13.01	20
D18:Y6	300	26.13	0.844	69.1	15.24	21
	350	26.26	0.845	67.8	15.04	21
D18:Y6:$PC_{61}BM$	350	26.82	0.861	70.1	16.19	21
PM6:Y6-BO-4Cl	300	26.40	0.831	69.75	15.31	22
PM6:PBB1-F:Y6-BO-4Cl	300	27.43	0.838	71.33	16.40	22
PM6:BTP-eC9	300	27.24	0.826	70.03	15.76	22
PM6:PBB1-F:BTP-eC9	300	27.71	0.836	72.69	16.84	22
D18:ZW1:Y6	300	27.52	0.831	72.9	16.67	23
	500	26.95	0.819	70.5	15.56	23
PM6:Y7-BO:Y6-1O	300	26.96	0.847	72.73	16.61	24
	360	26.89	0.842	71.67	16.23	24
	400	26.63	0.835	70.63	15.71	24
PM6:Y6	300	26.41	0.822	59.62	12.94	25
PM6:Y6:BTR-Cl	300	27.68	0.835	66.16	15.28	25
	500	23.83	0.826	56.63	11.15	25
PM6:BTR-Cl:Y6	297	29.2	0.767	61.7	13.8	26
PM6:BTR-Cl:CH1007	303	29.0	0.795	66.7	15.4	26
PM6:L8-BO	300	26.0	0.88	74.1	17.0	27
PM6:Y6	330	25.34	0.830	58.29	12.26	28
	460	24.17	0.823	56.91	11.32	28
PM6:Y6:F1	350	27.53	0.842	69.50	16.11	28
	480	27.08	0.834	67.43	15.23	28
PM6:L8-BO	300	26.5	0.90	74.5	17.8	29

DRTT-T:N3	300	22.00	0.85	58.5	10.89	30
DRTT-2Se:N3	300	23.33	0.85	66.9	13.20	30
DRTT-6Se:N3	300	25.53	0.84	64.3	13.81	30
PM6:L8-BO	250	27.30	0.88	69.0	16.44	31
PM6:BTP-eC9	300	27.64	0.820	68.9	15.62	32
	500	26.13	0.818	61.5	13.14	32
PM6:BTP-eC9:L8-BO-F	300	28.27	0.837	71.5	16.92	32
	500	27.40	0.836	63.1	14.45	32
PM6:BTP-eC9:L8-BO-F(LBL)	300	28.36	0.836	73.0	17.31	32
	500	27.49	0.835	66.4	15.21	32
PM6:L8-BO:DY-TF	300	27.80	0.884	74.18	18.23	33
	400	26.60	0.884	73.36	17.25	33
	500	25.80	0.883	69.83	15.91	33

Table S3. Mobility values of the devices at 300±10 nm thicknesses.

	Thickness (nm)	additives	μ_e ($cm^2\ V^{-1}\ s^{-1}$)	μ_h ($cm^2\ V^{-1}\ s^{-1}$)
PM6:L8-BO	300±10	NO	7.61×10^{-5}	1.06×10^{-4}
		DIO	1.12×10^{-4}	3.64×10^{-4}
		DICO	6.02×10^{-4}	8.24×10^{-4}

Table S4. Electronic mobility values for the PM6:L8-BO-based devices at different temperatures.

Temperature	No	DIO	DICO
298 K	5.92×10^{-5}	1.02×10^{-4}	5.79×10^{-4}
273 K	5.06×10^{-5}	8.17×10^{-5}	4.51×10^{-4}
253 K	3.50×10^{-5}	5.81×10^{-5}	3.54×10^{-4}
233 K	2.26×10^{-5}	3.83×10^{-5}	2.71×10^{-4}
213 K	1.31×10^{-5}	2.90×10^{-5}	2.11×10^{-4}
193 K	7.34×10^{-6}	1.85×10^{-5}	1.10×10^{-4}
173 K	4.00×10^{-6}	9.92×10^{-6}	8.01×10^{-5}
153 K	1.60×10^{-6}	3.24×10^{-6}	2.66×10^{-5}
133 K	2.28×10^{-7}	8.53×10^{-6}	5.67×10^{-6}

Table S5. Detailed parameters of single exciton decay dynamic for neat films.

Materials	γ ($\times 10^{-8}$ cm^{-2} s^{-1})	t (ps)	D ($\times 10^{-2}$ cm^{-2} s^{-1})	LD (nm)
PM6 (No)	4.66	70	1.86	11.4
PM6(DIO)	8.31	74	3.33	15.7
PM6 (DICO)	8.95	93	3.35	18.2
L8-BO (No)	3.02	170	1.20	14.3
L8-BO (DIO)	5.06	185	2.01	19.3
L8-BO (DICO)	6.9	230	2.76	25.2

Table S6. Summary of optimized solar cell performance of bilayer CuSCN/acceptor cells. All cells were tested under standard illumination conditions of AM 1.5G (100 mW cm^{-2}).

Acceptor	Additives	J_{sc} [mA/cm^2]	J_{cal} [mA/cm^2]	V_{oc} [V]	FF [%]	PCE [%]
L8-BO	No	3.63	3.59	0.849	41.7	1.29
	DIO	4.16	4.13	0.836	45.3	1.58
	DICO	4.27	4.22	0.831	51.5	1.83

Table S7. Morphological information as revealed by the GIWAXS investigations.

Donor:Acceptor		Additives	Q (Å^{-1})	Distance (Å)	FWHM (Å^{-1})	CCL (Å)
PM6:L8-BO	OOP (010)	No	1.73	3.63	0.25	22.90
		DIO	1.74	3.61	0.24	23.96
		DICO	1.74	3.61	0.21	26.80
	IP (100)	No	0.28	22.1	0.11	48.51
		DIO	0.28	22.6	0.10	52.82
		DICO	0.27	23.5	0.10	62.79

Table S8. Fitting parameters of 1D GISAXS profiles of three OSCs.

Donor:Acceptor	Additives	ξ (Å)	D	η (Å)	Rg (nm)
PM6:L8-BO	No	524	2.99	68.3	14.5
	DIO	382	2.97	80.7	17.2
	DICO	305	2.99	101.4	21.6

Table S9. Contact angles of H_2O and CH_2I_2 droplet on top of PM6 and L8-BO neat films processed without additive, with DIO and with DICO.

Films	**additives**	θ_{CH2I2} (°)	θ_{H2O} (°)	γ (mN m^{-1})	χPM6:L8-BO
PM6	No	49.53	95.76	34.7	0.40
L8-BO		34.56	91.23	42.6	
PM6	DIO	51.33	94.83	33.6	0.75
L8-BO		32.88	95.77	44.4	
PM6	DICO	53.50	93.54	32.3	1.13
L8-BO		31.44	97.68	45.5	

Table S10. Photovoltaic parameters of OSCs with different donors and acceptors under illumination of AM 1.5 G, 100 mW/cm^2.

Donor: Acceptor	Additives	Thickness (nm)	J_{sc}[a] [mA/cm^2]	V_{oc}[a] [V]	FF[a] [%]	PCE[a] [%]
PM6: Y6 [b]	DIO [d]	100±10 [i]	27.06 (26.87±0.35)	0.821 (0.820±0.001)	73.9 (73.3±0.7)	16.4 (15.8±0.4)
	DICO [f]	100±10 [i]	27.39 (27.17±0.23)	0.830 (0.830±0.001)	78.5 (78.2±0.4)	17.8 (17.6±0.1)
		300±10 [j]	27.17 (26.92±0.28)	0.814 (0.813±0.002)	73.3 (72.7±0.6)	16.2 (15.9±0.2)
D18: Y6 [c]	DIO[d]	100±10 [h]	26.15 (26.01±0.27)	0.824 (0.825±0.001)	75.5 (75.0±0.6)	16.3 (16.1±0.2)
	DICO [f]	100±10 [h]	26.32 (26.12±0.34)	0.837 (0.837±0.002)	77.7 (77.2±0.6)	17.1 (16.9±0.3)
		300±10 [i]	26.14 (25.92±0.33)	0.820 (0.819±0.002)	71.3 (70.8±0.4)	15.3 (15.0±0.2)
D18: L8-BO [c]	DIO [d]	100±10 [h]	25.86 (25.62±0.37)	0.863 (0.863±0.001)	76.6 (76.1±0.5)	17.1 (16.8±0.4)
	DICO [f]	100±10 [h]	26.17 (25.92±0.23)	0.884 (0.882±0.001)	80.0 (79.8±0.3)	18.5 (18.2±0.2)
		300±10 [i]	25.98 (25.72±0.34)	0.872 (0.873±0.003)	73.4 (73.1±0.4)	16.6 (16.4±0.2)

PM6: A-C10ch [b]	DIO [d]	100±10 [i]	26.42 (26.18±0.33)	0.833 (0.833±0.002)	74.6 (74.3±0.3)	16.4 (16.2±0.2)
	DICO [f]	100±10 [i]	26.86 (26.62±0.24)	0.860 (0.860±0.001)	78.3 (78.0±0.3)	18.1 (17.9±0.1)
		300±10 [j]	26.65 (26.32±0.38)	0.846 (0.844±0.002)	73.4 (72.9±0.5)	16.6 (16.2±0.3)
PM6: BTP-4F-P2EH [b]	DIO [d]	100±10 [i]	25.92 (25.63±0.34)	0.830 (0.830±0.002)	71.8 (71.2±0.6)	15.5 (15.1±0.3)
	DICO [f]	100±10 [i]	26.51 (26.32±0.28)	0.861 (0.860±0.001)	76.5 (76.2±0.3)	17.5 (17.2±0.2)
		300±10 [j]	26.18 (25.82±0.33)	0.842 (0.841±0.001)	70.8 (70.5±0.3)	15.6 (15.3±0.2)
PBQx-TF: PY-IT [c]	DIO [e]	100±10 [i]	25.63 (25.42±0.23)	0.912 (0.911±0.002)	65.9 (65.3±0.5)	15.4 (15.1±0.2)
	DICO [g]	100±10 [i]	25.77 (25.48±0.31)	0.920 (0.921±0.001)	69.5 (69.1±0.3)	16.5 (16.2±0.2)
		300±10 [j]	25.00 (24.75±0.28)	0.910 (0.910±0.002)	63.7 (63.2±0.4)	14.5 (14.2±0.3)
PM6: PYF-T-o [c]	DIO [e]	100±10 [i]	25.09 (24.85±0.26)	0.880 (0.880±0.001)	65.5 (65.0±0.4)	14.5 (14.2±0.2)
	DICO [g]	100±10 [i]	25.49 (25.25±0.31)	0.906 (0.906±0.001)	68.3 (67.9±0.5)	15.8 (15.5±0.1)
		300±10 [j]	24.82 (24.59±0.28)	0.892 (0.893±0.002)	62.7 (62.2±0.4)	13.9 (13.7±0.1)
PM6: IT-4F [b]	DIO [d]	100±10 [k]	21.26 (21.05±0.21)	0.832 (0.831±0.001)	73.8 (73.2±0.6)	13.1 (12.8±0.2)
	DICO [f]	100±10 [k]	21.63 (21.21±0.33)	0.842 (0.842±0.002)	75.0 (74.4±0.5)	13.7 (13.3±0.3)
		300±10 [l]	20.51 (20.25±0.28)	0.818 (0.817±0.001)	67.6 (67.2±0.4)	11.3 (11.1±0.1)

[a]The average values were obtained by measuring the parameters on 16 devices, [b]D:A = 1:1.2 (weight ratio). [c]D:A = 1:1.4 (weight ratio). [d]0.25% DIO (v/v). [e]1% DIO (v/v). [f]0.5% DICO (v/v). [g]2% DICO (v/v). [h]Donor concentration = 3.5 mg/mL in CF, followed by 100°C TA treatment for 3 min. [i]Donor concentration = 7.0 mg/mL in CF, followed by 85°C TA treatment for 5 min. [j]Donor concentration = 10.0 mg/mL in CF, followed by 100°C TA treatment for 5 min. [k]Donor concentration = 7.0 mg/m in CB, followed by 100°C TA treatment for 5 min. [l]Donor concentration = 10.0 mg/mL in CB, followed by 100°C TA treatment for 10 min.

Table S11. Optimized solar cell performance of the bilayer CuSCN/acceptor cells. All cells were tested under standard illumination of AM 1.5G (100 mW/cm^2).

Acceptor	Additives	J_{sc} [mA/cm^2]	J_{cal} [mA/cm^2]	V_{oc} [V]	FF [%]	PCE [%]
Y6	DIO	4.80	4.80	0.801	49.68	1.91
	DICO	5.02	4.95	0.809	52.76	2.14
A-C10ch	DIO	4.48	4.34	0.826	43.77	1.62
	DICO	4.66	4.55	0.829	46.08	1.78
BTP-4F-P2EH	DIO	4.30	4.23	0.831	34.48	1.23
	DICO	4.45	4.38	0.838	46.51	1.73
PY-IT	DIO	2.44	2.39	0.906	24.81	0.55
	DICO	2.56	2.45	0.914	38.04	0.89
PYF-T-o	DIO	2.34	2.31	0.874	26.75	0.55
	DICO	2.52	2.48	0.889	26.90	0.60
IT-4F	DIO	3.78	3.66	0.811	40.36	1.24
	DICO	3.92	3.80	0.808	52.06	1.65

Supplementary references

1. Lee, J. et al. Highly crystalline low-bandgap polymer nanowires towards high-performance thick-film organic solar cells exceeding 10% power conversion efficiency. *Energy Environ. Sci.***10**, 247–257 (2017).

2. Liu, X. et al. Low band gap conjugated polymers combining siloxane-terminated side chains and alkyl side chains: side-chain engineering achieving a large active layer processing window for PCE > 10% in polymer solar cells. *J. Mater. Chem. A* **5**, 17619–17631 (2017).

3. Fan, Q. et al. Synergistic effect of fluorination on both donor and acceptor materials for high performance non-fullerene polymer solar cells with 13.5% efficiency. *Sci. China Chem.* **61**, 531–537 (2018).

4. Gao, W. et al. Thick-Film Organic Solar Cells Achieving over 11% Efficiency and Nearly 70% Fill Factor at Thickness over 400 nm. *Adv. Funct. Mater.* **30**, 1908336 (2020).

5. Luo, Z. et al. Side-chain impact on molecular orientation of organic semiconductor acceptors: high performance nonfullerene polymer solar cells with thick active layer over 400 nm. *Adv. Energy Mater.* **8**, 1800856 (2018).

6. Wang, Z. et al. Significantly enhanced electron transport of a nonfullerene acceptor in a blend film with a high hole mobility polymer of high molecular weight: thick-film nonfullerene polymer solar cells showing a

high fill factor. *J. Mater. Chem. A* **8**, 7765–7774 (2020).

7. Weng, K. et al. High-efficiency organic solar cells with wide toleration of active layer thickness. *Sol. RRL* **4**, 2000476 (2020).

8. Ma, L. et al. A ternary organic solar cell with 300 nm thick active layer shows over 14% efficiency. *Sci. China Chem.* **63**, 21–27 (2019).

9. Jia, T. et al. 14.4% efficiency all-polymer solar cell with broad absorption and low energy loss enabled by a novel polymer acceptor. *Nano Energy* **72**, 104718 (2020).

10. Xiao, M. et al. Low temperature processed high-performance thick film ternary polymer solar cell with enhanced stability. *Nano Energy* **48**, 53–62 (2018).

11. Gao, J. et al. Over 14.5% efficiency and 71.6% fill factor of ternary organic solar cells with 300 nm thick active layers. *Energy Environ. Sci*.**13**, 958–967 (2020).

12. Zhan, L. et al. Over 17% efficiency ternary organic solar cells enabled by two non-fullerene acceptors working in an alloy-like model. *Energy Environ. Sci.***13**, 635–645 (2020).

13. Zhou, Z. et al. High-efficiency small-molecule ternary solar cells with a hierarchical morphology enabled by synergizing fullerene and non-fullerene acceptors. *Nat. Energy* **3**, 952–959 (2018).

14. Zhang, Y. et al. High performance thick-film nonfullerene organic solar cells with efficiency over 10% and active layer thickness of 600 nm. *Adv. Energy Mater.* **9**, 1902688 (2019).

15. Liu, Y. et al. Aggregation and morphology control enables multiple cases of high-efficiency polymer solar cells. *Nat. Commun.* **5**, 5293 (2014).

16. Pan, F. et al. Binary nonfullerene polymer solar cells with 430 nm thick active layer showing 15.39% efficiency and 73.38% fill factor. *J. Mater. Chem. A* **9**, 7129-7136 (2021).

17. Jin, Y. et al. Thick Film Polymer Solar Cells Based on Naphtho[1,2-c:5,6-c]bis[1,2,5]thiadiazole Conjugated Polymers with Efficiency over 11%. *Adv. Energy Mater.* **7**, 1700944 (2017).

18. Wang, Z. et al. Organic solar cells based on high hole mobility conjugated polymer and nonfullerene acceptor with comparable bandgaps and suitable energy level offsets showing significant suppression of J_{sc}-V_{oc} trade-off. *Solar RRL* **3**,100079 (2019).

19. Gokulnath, T. et al. Nonhalogenated solvent-processed thick-film ternary nonfullerene organic solar cells with power conversion efficiency >13% enabled by a new wide-bandgap polymer. *Sol. RRL* 2000787 (2021).

20. Li, Y. et al. Subtle side chain triggers unexpected two-channel charge transport property enabling 80% fill 44 factors and efficient thick-film organic photovoltaics. *The innovation* **2**, 100090 (2021).

21. Qin, J. et al. Over 16% efficiency from thick-film organic solar cells. *Sci. Bull.* **65**, 1979–1982 (2020).

22. Wang, J. et al. Synergetic Strategy for Highly Efficient and Super Flexible Thick-film Organic Solar Cells. *Adv. Energy Mater.* **12**, 2201614 (2022).

23. Zou, W. et al. A Bithiazole-Substituted Donor for High-Efficiency Thick Ternary Organic Solar Cells via Regulation of Crystallinity and Miscibility. *Adv. Energy Mater.* **13**, 2300784 (2023).

24. Bai, H. et al. Isogenous Asymmetric–Symmetric Acceptors Enable Efficient Ternary Organic Solar Cells with Thin and 300 nm Thick Active Layers Simultaneously. *Adv. Funct. Mater.* **32**, 2200807 (2022).

25. Zhang, L. et al. Regulation of Crystallinity and Vertical Phase Separation Enables High-Efficiency Thick Organic Solar Cells. *Adv. Funct. Mater.* **32**, 2202103 (2022).

26. Zhao, H. et al. High-Performance Green Thick-Film Ternary Organic Solar Cells Enabled by Crystallinity Regulation. *Adv. Funct. Mater.* **32**, 2210534 (2022).

27. Song, X. et al. Process-Aid Solid Engineering Triggers Delicately Modulation of Y-Series Non-Fullerene Acceptor for Efficient Organic Solar Cells. *Adv. Mater.* **34**, 2200907 (2022).

28. Zhao, F. et al. Fullerene-Liquid-Crystal-Induced Micrometer-Scale Charge-Carrier Diffusion in Organic Bulk Heterojunction. *Adv. Mater.* **35**, 2210463 (2023).

29. Song, X. et al. Film-formation dynamics coordinated by intermediate state engineering enables efficient thickness-insensitive organic solar cells. *Energy Environ. Sci.***16**, 3441-3452 (2023).

30. Cheng, X. et al. "Twisted" small molecule donors with enhanced intermolecular interactions in the condensed phase towards efficient and thick-film all-small-molecule organic solar cells. *J. Mater. Chem. A* **11**, 13984–13993 (2023).

31. Ding, G. et al. Solid Additive-Assisted Layer-by-Layer Processing for 19% Efficiency Binary Organic Solar Cells. *Nanomicro Lett* **15**, 92 (2023).

32. Cai, Y. et al. Vertically optimized phase separation with improved exciton diffusion enables efficient organic solar cells with thick active layers. *Nat. Commun.* **13**, 2369 (2022).

33. Wei, Y. et al. Over 18% Efficiency Ternary Organic Solar Cells with 300 nm Thick Active Layer Enabled by An Oligomeric Acceptor. *Adv. Mater.* 2304225 (2023).